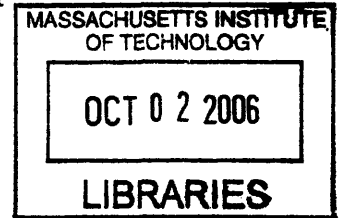# Time-resolved Spectroscopic Characterization of Ballistic Impact Events in Polymer and Nanocomposite Materials

by

Gagan Saini

Submitted to the Department of Materials Science and Engineering
in partial fulfillment of the requirements for the degree of

MASTER OF SCIENCE IN MATERIALS SCIENCE AND ENGINEERING

at the

MASSACHUSETTS INSTITUTE OF TECHNOLOGY

[September 2006]
August 2006

Author ....
Department of Materials Science and Engineering
August 14, 2006

Certified by ....
Keith A. Nelson
Professor of Chemistry
Thesis Supervisor

Certified by ....
Edwin L. Thomas
Head of the Department
Morris Cohen Professor of Materials Science and Engineering
Thesis Reader

Accepted by ....
Samuel M. Allen
POSCO Professor of Physical Metallurgy
Chair, Departmental Committee on Graduate Students

Time-resolved Spectroscopic Characterization of Ballistic Impact Events in Polymer and Nanocomposite Materials

by

Gagan Saini

Abstract

A detailed understanding of how materials respond to ballistic shock-loading is critical for the design and development of new protective materials. However, the nonlinear viscoelastic deformation present in polymers and nanocomposites during and immediately following a ballistic impact event is not currently well understood. The dynamic mechanical responses of materials experiencing ballistic shock-loading conditions are quite complex, with large amplitude compressions resulting in strain rates in excess of 10^6 s^{-1} and pressures exceeding several GPa. Historically, if one wants to study materials under ballistic shock loading conditions, a gas gun apparatus is necessary to generate appropriate high strain rate events. However, advances in high power ultrafast laser amplifier systems have opened the possibility of optically generating ballistic shocks which are comparable to a shock wave generated by gas gun apparatus.

Time-resolved mechanical property information, such as elastic modulus, bulk modulus, shear modulus, and Poisson's ratio are measured using impulsive stimulated thermal scattering, a laser-based photoacoustic technique. A series of polymeric and polymer based nanocomposite material systems are studied, including multilayered thin films of alternating layers of polymer and hard nanoparticles, un-annealed and fully annealed poly(methyl methacrylate) (PMMA)–polyisoprene block copolymer thin films, and polyhedral oligomeric silsesquioxane (POSS) doped PMMA thin films. The experimental results on these materials clearly demonstrate that this technique is sensitive enough to measure mechanical property differences in samples with only small compositional or structural changes. Since the data can be acquired in real time, or a single shot basis, the measurement is compatible with laser shock loading of the sample. This is demonstrated by preliminary experimental results.

Thesis Supervisor: Keith A. Nelson
Title: Professor of Chemistry

Acknowledgments

I strongly believe that perfection is already there in man, inherent in his heart and soul, and education is the medium through which we are able to manifest that perfection in us. I also do believe that scientific research is one area that stretches one's mental faculties beyond the realms of conventional thinking and enables the probing and answering of new queries in the never ending deep quest for knowledge. There are people that have helped while working on the projects mentioned in this thesis, and their contributions are greatly appreciated.

My thesis advisor, *Professor Keith A. Nelson*, has been integral in the development of my scientific capacity. He showed incredible faith in me, and recognized the value of independence. He built my self-confidence by trusting me to lead the project by my own. His vast research experience and scientific intuition have taught me to ask the right questions and to think more critically. I am also grateful to *Professor Edwin L. Thomas*, who has been actively involved with the project as the director of the Institute for Soldier Nanotechnologies (ISN) and also in capacity as my thesis reader. His fundamental understanding of polymer physics and processing continues to serve as an excellent source of clarification and insight.

I was fortunate enough to work with a postdoctoral associate, *Dr. Emmanuel Peronne* who helped me to build the experimental set-up and taught me the basics of linear and non-linear optics. *Dr. Thomas Pezeril*, another postdoctoral associate, has been incredible in helping to take and analyze data. His strong theoretical background and experimental finesse have helped to answer some puzzling questions. He has spent many hours in the lab with me, laboring over alignment and dismal signal quality. He is my mentor as well as my good friend and we have spend good and bad times together. *Dr. Steven Kooi*, who is a research scientist at ISN, has been a constant source of help to me and I admire his relentless patience in working on alignment of laser systems. I also do share many scientific and non-scientific opinions on different matters with him. *Cindy Bolme*, who was working on this project earlier, is always happy to answer any queries I have related to the experiment and she helped me a lot when I visited her at Los Alamos National Laboratories. I would like to thank *Dr. Jongseung Yoon* for sample preparation, *Dr. Vahik Krikorian* for helping me with TEM imaging, and *Sharon Soong* for conducting DMA experiments on my samples.

I have been blessed with a wonderful research group. The group also actively contributed to the development of this work, through fruitful discussions and interactions that helped me shape this work. I am particularly grateful to *Darius Torchinsky* who was always supportive in helping me with experiments and data collection. I feel happy to call him my *secondary advisor*. I would also like to thank *Neal Vachhani*

for helping with sample preparation, characterization and design of the experiment. His innovative ideas to prepare new samples were truly appreciable. We spent a good amount of time thinking about the sample geometry and selection of materials for the experiment. Finally, I would like to thank the U.S. Army Research Office for their generous and continued support under contract DAAD–19–02–D–0002, of the ISN at MIT.

My loving mother and younger brother continue to be my inspiration and source of endless support. *I would like to dedicate this thesis to my beloved father, Dr. Om Prakash Saini whom I lost two years back. I will always miss you Dad !*

Contents

List of Figures

10

List of Tables

Chapter 1

Introduction

The nonlinear viscoelastic deformation mechanisms and dynamics in polymers during and immediately following ballistic or blast events remain obscure. Polymers exhibit strong rate-dependent mechanical behavior and in different frequency regimes, the rate sensitivities of polymers change as various primary (α) and secondary (β) molecular mobility mechanisms are accessed. A soft, free-flowing sand is effective against impacts of a velocity close to 1 mile/s (30-caliber bullet speed). On the other hand, a simple knife can defeat the sand bag. Studying the dynamical mechanical behavior within the shocked region requires specialized techniques and diagnostic equipment. Moreover, inertia and inner kinetics of materials become an important factor and dynamical deformation often involves wave propagation [1].

This thesis aims to investigate the response to laser-generated shock of various material systems, ranging from amorphous homopolymers to nanostructured polymer-based composites. Regardless of whether a shock wave is laser-driven or results from being inside the blast radius of an improvised explosive device (IED), the impacted material still experiences rapid delivery of high mechanical energy density. Accordingly, the response of a candidate armor material, a biological tissue, or a novel fabric

component, tested on micron size scales, could reveal much about its response on macroscopic size scales. The mechanical behavior under laser-shock conditions is quite complex, with shock pulses lasting a few nanoseconds, delivering strain rates of $10^8 \, \mathrm{s}^{-1}$ and pressures exceeding several GPa. These conditions even exceed those imposed during blast and ballistic events, where strain rates of $10^5 \, \mathrm{s}^{-1}$ and $10^6 \, \mathrm{s}^{-1}$ are regularly achieved, albeit with thicker targets. In thin targets the entire impacted target region distorts while in thick ones the region near the impact remains intact and distortion of the impacted region takes place through internal modes rather than translation of the whole target region.

The characterization of polymeric materials subject to shock loading is germane to the development of high-performance engineering materials. This is especially important for soldier armor for personnel protection, since blunt trauma affects human tissue, organs, biopolymers, and gels. There is still much to be learned about the response of soft matter to violent impacts. To this end, a novel pairing of optical shock generation and time-resolved spectroscopy is used, providing an insightful tool for studying the time-dependent material response to large-amplitude short-time mechanical transients. The synergy in their combination allows for observation of relaxation dynamics at fast time-scales. We use impulsive stimulated thermal scattering (ISTS) to study the propagation of bulk and surface in-plane and through-plane acoustic waves in shocked polymeric materials. A comprehensive set of mechanical properties including elastic, shear and bulk modulus as well as Poisson's ratio are obtained by fitting experimental data to a model for acoustic dispersion curves. The temporal history of structural relaxation and dynamic behavior helps to depict modes of energy dissipation through the material. The dynamics of structural changes induced by ballistic impact and the dissipation of mechanical energy on the time scale of the shock event are of obvious concern for the design and effectiveness of protective

16

materials.

This thesis is the beginning of a broader investigation that aims to better understand energy propagation and energy dissipation in polymeric materials at blast frequencies. The approach is to establish the compatibility of the photoacoustic technique, ISTS to allow probing of nanoscale structures and their dynamical mechanical responses to ballistic impact loading.

Chapter Two provides details of the ISTS set-up and measurements on a number of samples including a multilayer sample that shows interesting acoustic properties. These measurements are interesting in their own right, and they also are conducted with a sample configuration (polymer sandwiched between aluminum and gold layers, all on a bulk substrate) that permits coupling to laser shock generation. Chapter Three presents a fundamental technical overview of shock theory and methods of shock characterization. In Chapter Four, I have demonstrated laser shock generation in sample structures like that described above, and obtained preliminary results indicating successful ISTS measurements in a sample under shock loading. This chapter puts the current and planned work in context with prior work done in shock wave spectroscopies. Chapter Five outlines the conclusions drawn and makes suggestions for future work.

Chapter 2

Impulsive Stimulated Thermal Scattering (ISTS) or Transient Grating (TG) Photoacoustics

2.1   Introduction

The determination of thermal and mechanical properties of thin films is of great technological significance for polymer, micro-electronics, defense and bio-medical applications. Many different techniques have been used including dynamic mechanical analysis (DMA), heat capacity and thermal conductivity measurement methods, ultrasonics and optical or non-contact methods. Brillouin spectroscopy, picosecond laser pulses to excite longitudinal waveguide modes [2], and impulsive stimulated thermal scattering (ISTS) or transient grating (TG) photoacoustics are optical methods used to determine transverse and longitudinal acoustic wave properties. In this thesis, the ISTS technique is used to generate data from which relevant thin film properties of novel materials can be evaluated. Other techniques require long data collection times,

19

thin films, small acoustic damping rates and acoustic impedance matching and hence pose a great limitations in many systems to be studied [3].

ISTS is a non–contact, accurate, fast and non-destructive tool for the characterization of acoustic waves in films – single or multilayer. In ISTS, two short excitation pulses (preferably pico or femtosecond) derived from the same laser via diffraction of +1 and -1 orders of a 1D linear phase mask, are crossed spatially and temporally in an absorbing sample to form an optical interference pattern (See Figure 2-1). The phase mask used in our work is a periodic grating of grooves etched into silica. Optical absorption at the interference maxima leads to mild, spatially periodic sample heating, and thermal expansion at the heated regions launches coherent monochromatic counter-propagating surface acoustic waves forming transient diffraction grating [4, 5]. The magnitude of the in-plane acoustic wavevector, k, is given by

$$k = \frac{4\,\pi\,\sin(\theta_E/2)}{\lambda_E} \tag{2.1}$$

where λ_E is the wavelength of the excitation pump light and θ_E is the crossing angle between the two excitation pulses at the surface of thin film.

The acoustic wavelength, λ_a, due to the excitation interference pattern is equal to the interference fringe spacing, and is given by

$$\lambda_a = \frac{2\,\pi}{k} = M\,\frac{d}{2} \tag{2.2}$$

where d is the grating spacing of the phase mask pattern, k is given by Equation (2.1) and M is the magnification ratio of the imaging system ($M = f/(o - f)$, f is the focal length and o is the object (phase mask in our case) distance from the lens).
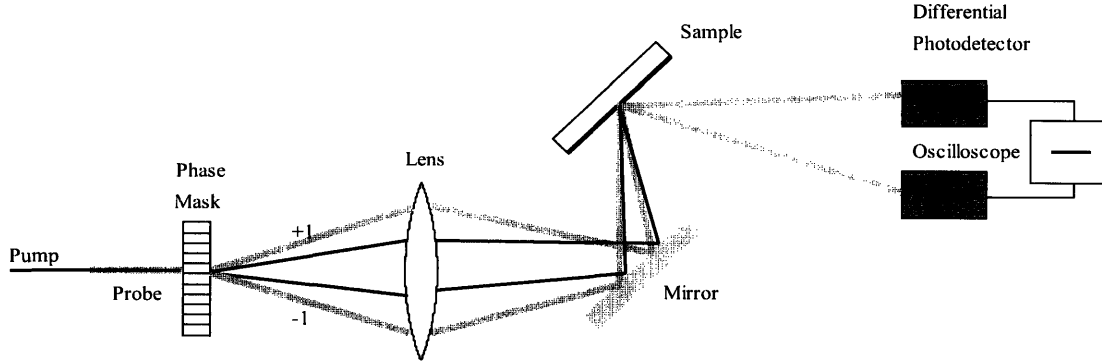
Figure 2-1: Schematic of the Impulsive Stimulated Thermal Scattering (ISTS) or Transient Grating (TG) photo acoustics experiment. The pump pulses are 200 fs in duration and 400 nm in wavelength, generated using an amplified Ti:sapphire laser system. The continuous wave Nd:YAG probe laser beam has 532 nm wavelength.

The continuous wave (cw) probe beam and a pulsed pump beam are collinear and overlap at the phase mask as shown in the schematic illustration of the ISTS set–up in Figure 2-1. The +1 and -1 order diffracted pump beams are recombined at the sample to generate the acoustic waves. The two diffracted probe beams are used for phase-stabilized optical heterodyne detection [6]. Each probe beam is coherently scattered or diffracted into the path of the other by the acoustic diffraction grating and the superposed optical fields are detected and subtracted, revealing damped acoustic oscillations on nanosecond time scales, i.e. typically 100 MHz – 1 GHz and potentially ~30 MHz – 3 GHz acoustic frequencies. This diffracted signal is collected by fast detection electronics comprised of amplified photodiodes and a transient digitizing oscilloscope to resolve the time-dependent material response. The major limiting factors in ISTS time-domain spectroscopy are limited time resolution, given by the detection electronics, and limited wavevector range, given by the range of interference fringe spacings (roughly 2-200 microns) that can be achieved with optical pump beams and the available phase masks. However, it permits generation of tunable, narrowband in-plane acoustic waves with frequencies up to a few GHz.

21

An acoustic dispersion curve (variation of phase velocity with respect to acoustic wavevector) is generated by changing the grating spacing through translation of the phase mask substrate, which contains about 20 patterns that are optimized for diffraction at the wavelength of the excitation laser [7, 8]. The study of propagation of pseudo-Rayleigh and pseudo-Lamb acoustic waveguide modes in supported and free-standing layered films respectively, can be used to determine the intrinsic mechanical properties of materials in the particular structure or configuration [9, 10]. There is a strong dependence of the acoustic frequency on the elastic properties, density, thickness and mechanical boundary conditions (e.g. substrate adhesion or delamination) of each film in a multilayer stack. Hence, the measurement of multiple acoustic waveguide modes and their dispersion reveal acoustic behavior which can then be used to extract the elastic properties of the film. The detailed quantitative theory of ISTS acoustic excitation and probing processes are discussed in papers by Yan, Duggal, Rogers and Nelson [11, 12, 13, 14, 15, 4]. For thin films in a multilayer, boundary conditions at the interfaces lead to coupling between longitudinal and transverse potentials and hence every surface acoustic mode has both longitudinal and transverse character.

The time-dependent acoustic and thermal ISTS response, $I_S(t)$, is given by

$$I_S(t) = A \left[e^{-t/\tau_{th}} - e^{-t/\tau_{ac}} cos(2\pi f t) \right] \tag{2.3}$$

where A is the strength or amplitude of the signal, τ_{th} is thermal diffusion time, and τ_{ac} is apparent acoustic damping rate.

ISTS response contains a single amplitude term A that multiplies both dynamical parts, thermal diffusion and acoustic responses (See Equation 2.3). The total response consists of a steady-state response, the thermal expansion, and a transient

response, the acoustic oscillations, the latter arising because the driving force is sudden and the response overshoots the steady-state value, by exactly the steady-state amplitude amount, so we have oscillations between the acoustic maximum and zero about the steady-state amplitude until they are acoustically damped, then on longer time scales thermal diffusion from grating peak to null removes the steady-state response. Equation 2.3 is used to extract acoustic parameters, thermal diffusivities and thermal conductivities.

For thin film irradiation, the effective ISTS time-independent acoustic amplitude, A can be nominally described as:

$$A \propto \frac{\beta(1 - R_\lambda)Q}{\rho\, c_P\, S\, d} \tag{2.4}$$

where β=linear thermal expansion coefficient, R_λ=reflectance at excitation wavelength λ, Q=excitation pulse energy, ρ=density, d=depth over which the heat is deposited (which is equal to film thickness if the film is fairly thin and the heat is deposited fairly uniformly across it), c_P=heat capacity, and S=spot size.

The precise nature of the displacements in a film-substrate assembly will depend on important details including the shear and bulk moduli of all the film layers and the substrate and on where the heat is deposited (e.g. only at the front of a thick layer, roughly uniformly throughout a thin layer, throughout many layers and the substrate surface, etc.). These factors determine the initial, impulsively imposed heat distribution, the anisotropic compressional and shear stress distributions resulting from it, and the projection of the overall response along different acoustic waveguide modes whose displacements relieve the stresses. Although these details are specific to each sample, the important general considerations concerning the amplitude of the response are the ones given in Equation 2.4, and the key information that we extract

23

is not going to come from precise determination of the acoustic amplitudes anyway but only from the dynamics of the response, i.e. acoustic frequencies and decay rates. The amplitude expression, Equation 2.4, is mainly important in guiding selection of a thin film material that will produce a strong overall ISTS signal level, not in guiding the detailed data analysis.

On the other hand, in some samples there is complex structural relaxation on a time scale that is long compared to the acoustic oscillation period but shorter than the thermal diffusion time. This makes it take longer to reach the steady-state thermal expansion response, and so the steady-state response then consists of a fast part A, which is still the acoustic amplitude, plus a slow part. The slow part would normally have some distinct dynamics associated with the slow structural relaxation, at the very least a single-exponential rise time [16, 9].

Values of material properties influence the ISTS signal intensity, based on Equation 2.4 for thermal expansion due to laser excitation. Gold produces a strong ISTS signal, since it exhibits a large amplitude signal A, and this is the reason we have an overlayer of gold on top of polymer for all samples studied by this technique. A polymer that absorbs the pump or excitation wavelength strongly and whose ISTS signal can be probed directly would not need the gold over layer for signal enhancement [17, 18, 19]. Another reason for the gold layer will emerge, namely in shock measurements (Chapter 4), it will protect the probe light from reaching the sample region underneath that has been irradiated by the shock laser pulse which destroys a separate metal layer and which could give rise to unwanted scattering of the probe light. Note that Equation 2.4 is actually specific to metals, or at least to a sample that either absorbs or reflects the entire pump light. For a polymer on glass, or some other potentially transparent sample, the factor $(1 - R_\lambda)$ would need be changed to $(1 - R_\lambda - T_\lambda)$ to include transmission (T_λ) through the sample as well as reflection off

it. The point is that this term is the fraction of the incident light that gets absorbed.

2.2   Experimental Set-up

Figure 2-1 shows the ISTS experimental arrangement in reflection geometry for opaque samples. The set-up has also been used in transmission mode for transparent materials. The pump and probe beams are focused onto the mask with spherical lenses (not shown in Figure 2-1). A phase mask is used to diffract the short excitation laser pulse (200 fs, λ=400 nm, 500 μJ, from an amplified Ti:sapphire laser system) into multiple orders. The phase mask or diffraction grating is designed to optimize the diffraction efficiency of incident pump light into the first ($\pm$ 1) diffraction orders. These first order diffraction maxima are recombined by a spherical lens that images the mask pattern onto the sample using a one-lens imaging system, while all the higher orders and the zero order beams are blocked by a spatial filter.

The excitation wavevector k can be easily varied between 1.5×10^5 m^{-1} and 1.5×10^6 m^{-1} by translating the phase mask to different etched patterns. The time-dependent material response is monitored by a cw probe laser beam (532 nm, 30 mW, Coherent Verdi) that is incident on the phase mask parallel to and directly above the excitation beam. The reflected part of each probe beam is collinear with and phase-coherent with the diffracted signal from the other probe beam, and the collinear probe and diffracted signal superpose to permit optical heterodyne detection of the signal. The signal from each beam is focused into one of two diodes in a custom-built differential detector (Cummings Electronics Labs., North Andover, MA). The signal is amplified and then averaged by a fast digitizing oscilloscope (Tektronix TDS 7404, 4 GHz).

The transient grating wavelengths generated by the different phase mask patterns were carefully calibrated to within 1% accuracy prior to the experiment, by making
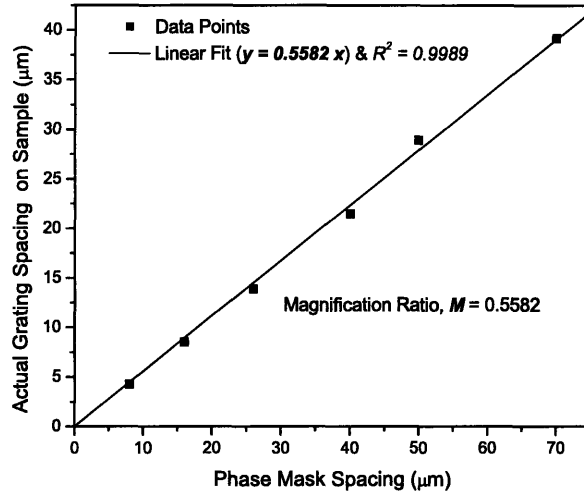
Figure 2-2: Calibration of transient grating spacing in ethylene glycol using a series of phase masks with different spatial periods. The imaging ratio for the one lens focusing system is 1:0.56.

ISTS measurements in ethylene glycol doped with 10^{-3}M Coumarin 515 laser dye at 294 K (room temperature) in transmission mode (See Figure 2-2). Ethylene glycol has a temperature-dependent acoustic velocity v near room temperature [20] given by

$$v\,(km/s) = 1.658 - 2.1 \times 10^{-3}\,(T - 298) \tag{2.5}$$

where T is the temperature in Kelvin.

2.2.1 Sample Specifications

Block copolymers and multi-component systems have received significant research interest over the past several decades because of the unique properties that these materials possess compared to their homopolymer components [21, 22]. The mechan-

26
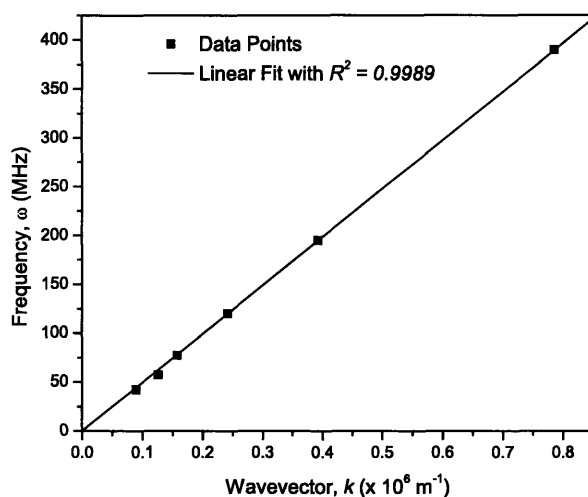
Figure 2-3: Dispersion relation showing acoustic wavevector versus frequency curve for ethylene glycol at 294 K. Notice the linear relationship suggesting zero dispersion or constant acoustic speed independent of wavevector in this range.

ical behavior of these materials can be markedly different from their exhibited by each individual neat component due to a wide range of self-assembled, ordered or partially ordered morphologies. This invites multidimensional optimization of mechanical properties for specialized applications based on the individual components and the manner in which they are combined. The morphology is strongly influenced by composition and processing conditions.

Poly(methyl methacrylate)–Polyisoprene (PMMA-b-PI) block copolymer is used to study the effect of annealing on mechanical behavior using ISTS technique. The glass transition temperature, T_g of PMMA and PI are 105 °C and -70 °C respectively [23]. Thus, PMMA behaves like a glassy solid and PI is a rubbery material at room temperature.

Nanocrystalline materials such as TiO_2 are particularly attractive for many engineering applications due to their intrinsic properties including transparency and rel-

$$-[CH_2-\underset{\underset{\underset{CH_3}{|}}{\overset{\overset{C=O}{|}}{O}}}{\overset{CH_3}{\underset{|}{\overset{|}{C}}}}]-$$

$$+CH_2\underset{H_3C}{\overset{}{C}}=\underset{H}{\overset{CH_2}{\overset{}{C}}}]_n$$

Poly(methyl methacrylate) or PMMA   Polyisoprene or PI

10-corner cage methacryl-Polyhedral oligomeric silsesquioxanes or POSS
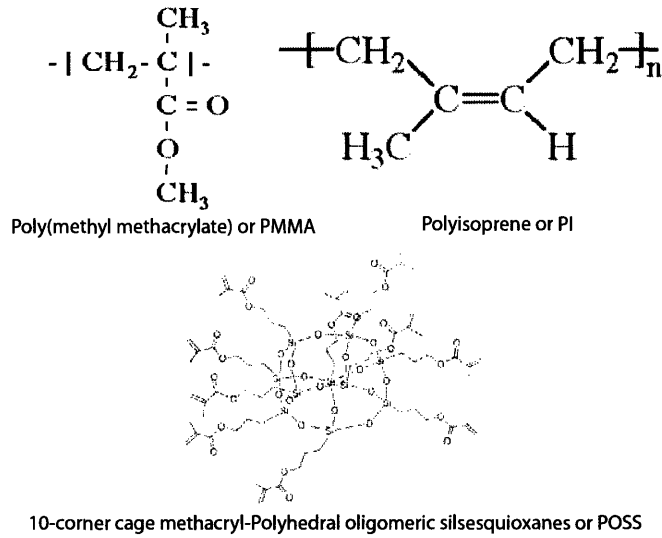
Figure 2-4: Molecular Structure of Poly(methyl methacrylate), Polyisoprene and methacryl–Polyhedral Oligomeric Silsesquioxanes (POSS) [27].

atively high moduli and due to their easy processability which enables a wide range of multicomponent morphologies whose properties may be varied systematically [24]. In multilayer systems with these components, it should be possible to control the mechanical behavior as well as acoustic properties including phase and group velocity dispersion and phononic bandgap structure by specifying the details of the two components and by varying the thickness of each individual layer and/or optimizing the number of layers [25]. A multilayer structure of PMMA and nanocrystalline TiO_2 is used as model system to understand the mechanical behavior of complex multilayer stacks. A better understanding of the mechanical properties of these types of systems will be used in the design of new materials for energy dissipation applications [26]. The acoustic dispersion curves of neat PMMA, neat TiO_2, and PMMA–TiO_2 multilayers are determined in order to characterize the evolution of mechanical properties of the multilayer structure.

Recent research interest has also included the use of nanomaterials to further ex-

plore and enlarge the property space of polymers. The incorporation of nanoparticles into the polymer matrix can potentially alter the local molecular level structure and thus offers an opportunity to tailor the rate-dependent mechanical deformation and failure behavior of the polymer [28]. Nanomaterials can be introduced into a polymer system by blending or chemical attachment. Blending is simple and can be done by physical means, but there may be solubility limits resulting in phase separation. In this study, a model group of nano-structured compounds known as polyhedral oligomeric silsesquioxanes (POSS) are dispersed at a level of 5 wt% in the PMMA matrix. The largest dimension of the methacryl-POSS molecule (obtained from Hybrid Plastics, Fountain Valley, CA) is approximately 2.5 nm as shown in Figure 2-4. POSS molecules feature an inorganic cage-like structure made of silicon and oxygen atoms, with different unreactive and/or functional organic groups connected to the corner silicon atoms. This methacryl-POSS is a non–crystallizable mixture of 8–, 10–, 12–, and 14–corner POSS cages, with 10–corner cages having the highest weight fraction. POSS can also be incorporated into homopolymers through direct blending though it tends to aggregate within a polymer matrix at higher weight fractions.
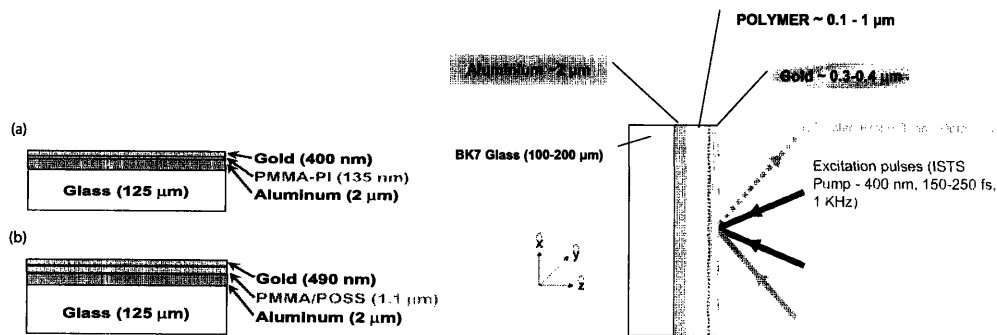

Figure 2-5: Left Figure: Depiction of sample assembly used for ISTS detection. (a) PMMA-PI block copolymer system and (b) PMMA/POSS polymeric system (not to scale). The gold layers are deposited using e-beam and polymer films are spin coated. Right Figure: General sample geometry along with pump and probe used for the measurement technique.

The Poly(methyl methacrylate)–Polyisoprene or PMMA–PI samples and PMMA/ POSS samples were spin-coated onto glass cover slips with $2\mu m$ thick aluminum layers, by spin coating (See Figure 2-5). The PMMA-PI Block copolymer and PMMA/POSS samples were 135 nm and $1.1\mu m$ thick respectively as measured using a mechanical stylus profilometer and ellipsometer. The molecular structures of the compounds are shown in Figure 2-4. The PMMA used in this study was custom-made by Scientific Polymer Products, Inc. (Ontario, NY) with an approximate molecular weight of 70,000 g/mol.

Inorganic titania (TiO_2) nanoparticles and PMMA have been employed as high and low elastic modulus materials respectively for constructing multilayer phononic structures. TiO_2 nanoparticles were prepared by the synthetic scheme of Sanchez et al [29]. The nanocrystalline TiO_2 particles were composed of anatase phase (refractive index ~1.85 at 500 nm) with an average diameter of about 1-5 nm. The TiO_2 particles were readily dissolved in polar organic solvents such as butanol due to an organic surface capping group, acetylacetone. PMMA (Aldrich, MW: 50,000 g/mol) was used as received and dissolved in toluene for making these samples. For fabrication of an organic/inorganic multilayer phononic structure, $(TiO_2–PMMA)_5$, solutions of TiO_2 (in butanol) and PMMA (in toluene) were alternately spin-coated on a glass substrate, with target thicknesses (110 nm (TiO_2) and 135 nm (PMMA)). The thicknesses were controlled by concentration of the solution, amount of solution, and/or spin speed. A final gold layer (130 nm thick) was deposited by e-beam so that the ISTS excitation pulses would be strongly absorbed and the probe light highly reflected.

2.3 Data Analysis

In this section, the longitudinal and the transverse acoustic velocities of the films are determined through fitting of theory to experiment. The acoustic waveguide modes in supported films, known as Rayleigh or Sezawa modes, are strictly guided for velocities less than the transverse acoustic velocity in the substrate [9, 10]. When the acoustic wavelength is long compared with film thickness, the effects of the film are small compared with those of the substrate. On the other hand, when the wavelength is short compared with the film thickness, the substrate has a small effect on the modes and the mode velocities approach the intrinsic transverse velocity of the film. There are many Rayleigh modes which can propagate on a layered medium and for a given system, the number of possible modes depends only on the product of the acoustic wavevector and the thickness of the film layer, i.e. on the ratio between the acoustic wavelength and the layer thickness.

ISTS photoacoustic measurements on polymeric samples were made using the experimental setup shown in Figure 2-1. Typical diffracted ISTS signals for thin film are shown in Figures 2-6, 2-7, 2-8, 2-9, and 2-10. The data shown represent averages over 1000 repetitive measurements. The acoustic response consisting of counter-propagating waves gives rise to damped oscillatory material motion on a nanosecond time scale and the thermal response gives rise to quasi-steady-state motion, which persists until thermal diffusion washes out the temperature grating, usually on many nanoseconds or microsecond time scales. The oscillations are associated with acoustic standing waves. The oscillation frequency depends upon the material's acoustic velocity and the decay rate depends upon the acoustic attenuation.

Measurement of multiple (or single) modes and their dispersion reveal the acoustic behavior of the film, which can be used to extract the elastic properties of the
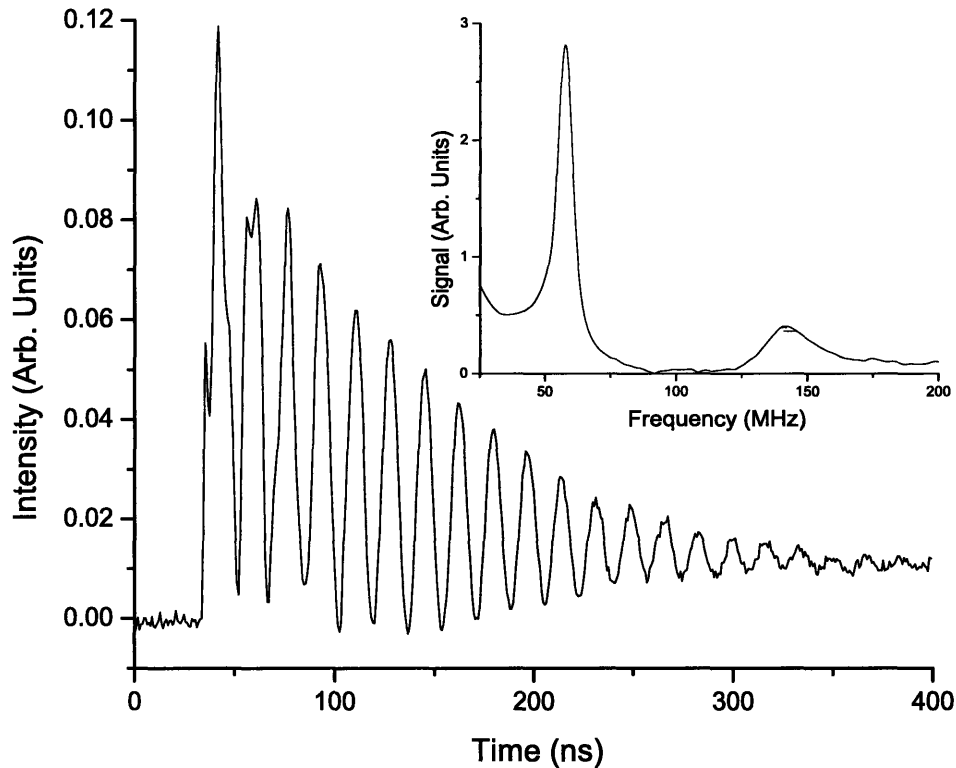
Figure 2-6: Diffracted ISTS signal from 1.1 μm polymer film sandwiched between gold and aluminum for neat PMMA (sample assembly shown in Figure 2-5(b)). The inset shows the Fourier transform of the diffracted ISTS signal and clearly illustrates the existence of multiple modes. The acoustic wavelength is 14.0 μm.

isotropic films. The analysis begins with the measurement of the temporal profile of the system at a range of acoustic wavelengths. Fourier transformation of the data yields the acoustic frequency at each wavelength and the dispersion curve as shown in Figures 2-12, 2-11, 2-13, and 2-14. Solutions of the thermoelastic equations of motion for a multilayer system have been used to develop numerical code that allows measured dispersion curves to be fit with variable material parameters to determine the parameter values. The sum of squared differences between the measured disper-
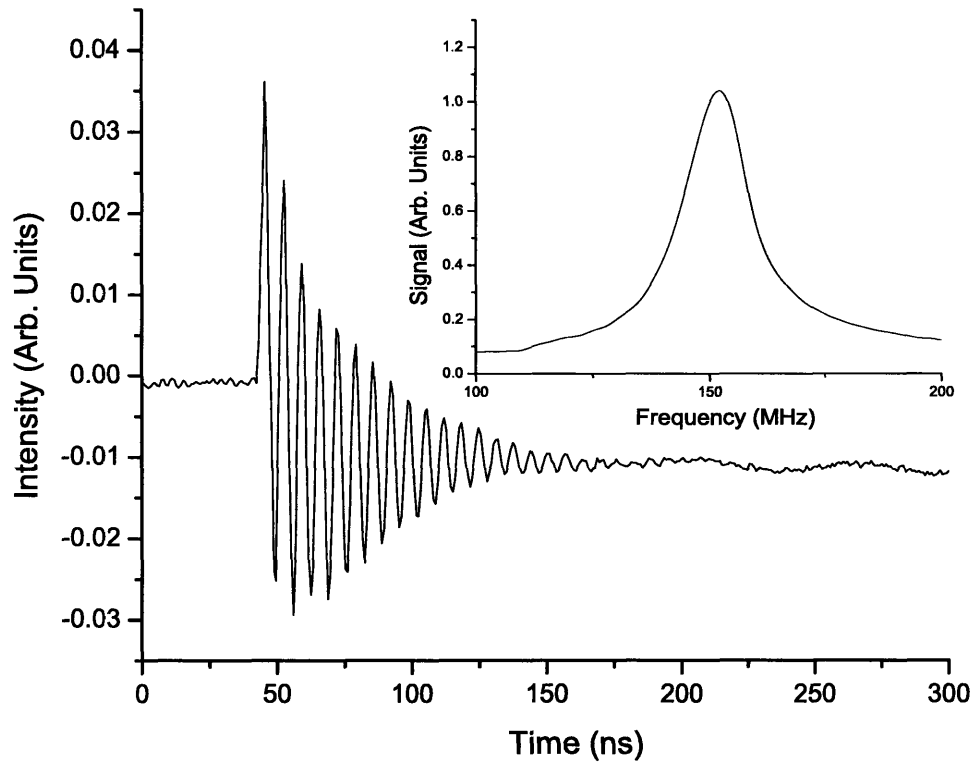
Figure 2-7: Diffracted ISTS signal from 1.1 μm polymer film sandwiched between gold and aluminum for PMMA–5 wt% POSS (sample assembly shown in Figure 2-5(b)). The inset shows the Fourier transform of the diffracted ISTS signal. The acoustic wavelength is 4.3 μm.

sion and calculations that assume values for the physical properties of the waveguide provides a metric for the quality of the model. Adjusting the parameter values (e.g. elastic moduli, densities, and thicknesses) to optimize the quality of the fit yields the characteristics of the unknown components of the film.
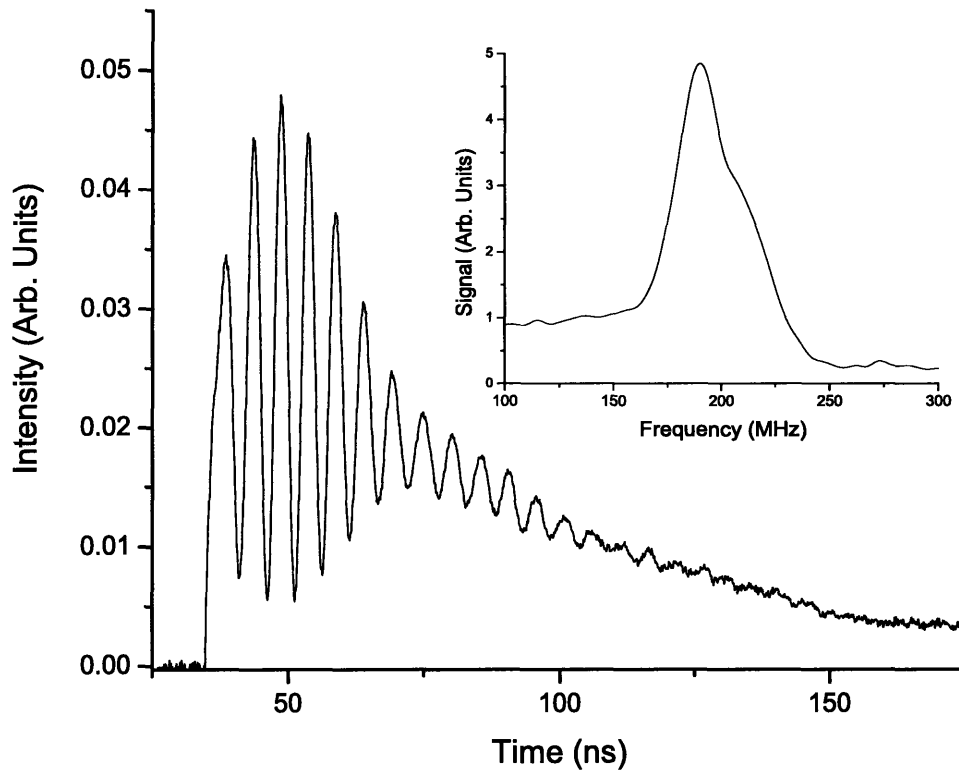
Figure 2-8: Diffracted ISTS signal from a 130 nm polymer film sandwiched between gold and aluminum for PMMA–PI block copolymer annealed for 5 hours (sample assembly shown in Figure 2-5(a)) at 10.8 μm acoustic wavelength. The inset shows the Fourier transform of the diffracted ISTS signal.
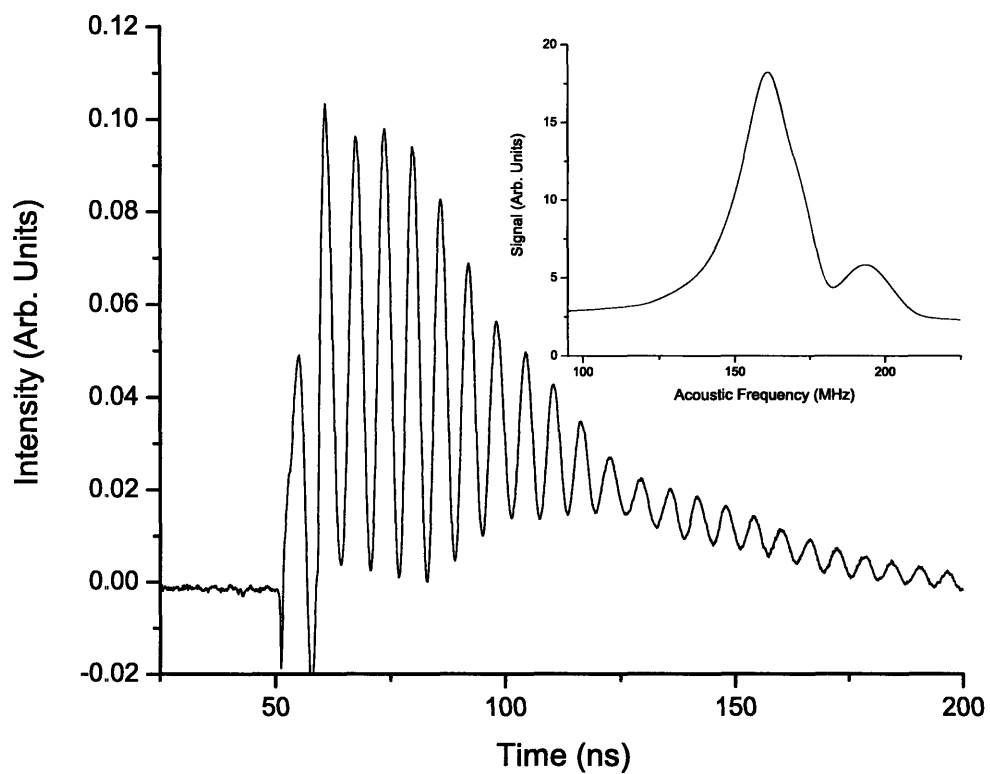
Figure 2-9: Diffracted ISTS signal from a 130 nm multilayer/lamellar polymer film sandwiched between gold and aluminum for PMMA–PI block copolymer annealed for 50 hours (sample assembly shown in Figure 2-5(a)) at 13.5 μm acoustic wavelength. The inset shows the Fourier transform of the diffracted ISTS signal and clearly illustrates the existence of two modes.

35
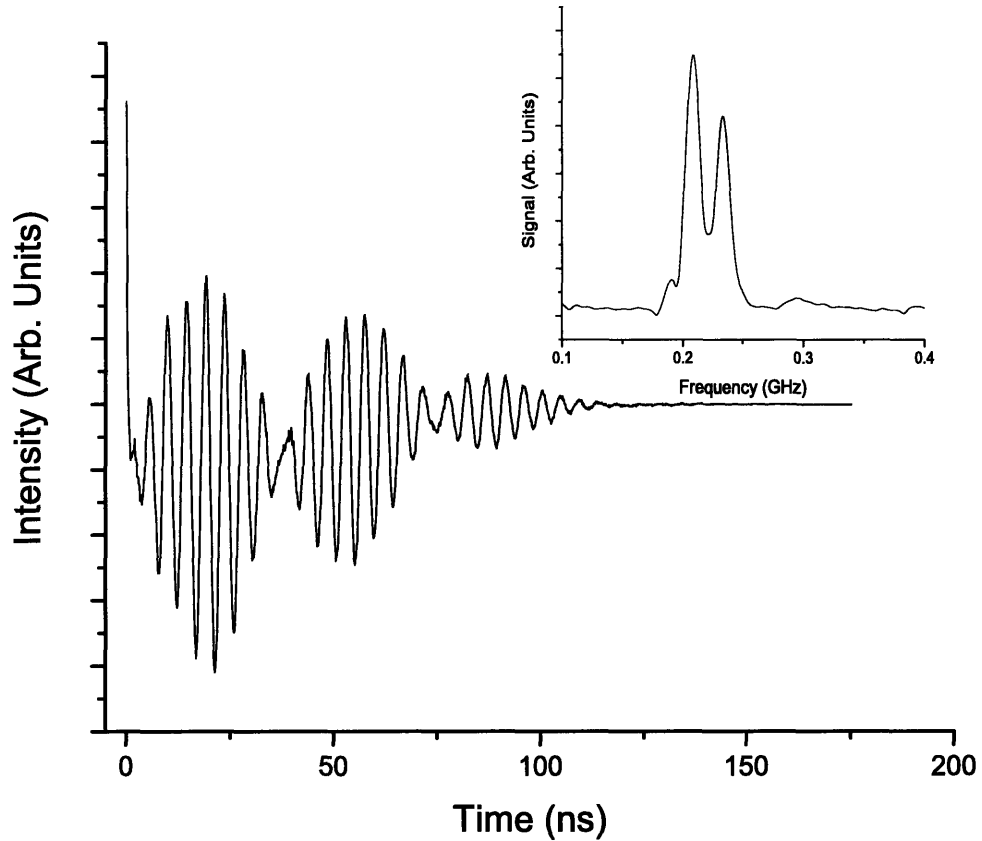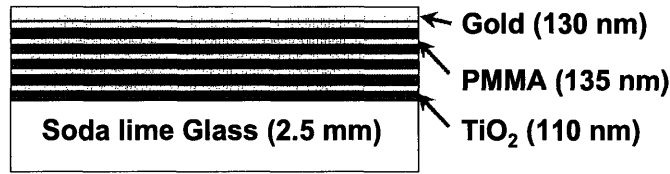
Figure 2-10: Top Figure: Depiction of sample assembly for PMMA-TiO$_2$ multilayer structure used for ISTS detection (not to scale). Bottom Figure: Diffracted ISTS signal from PMMA-TiO$_2$ multilayer film sandwiched between gold and glass at 12 μm acoustic wavelength. The inset shows the Fourier transform of the diffracted ISTS signal and clearly illustrates the presence of two thin film acoustic waveguide modes.
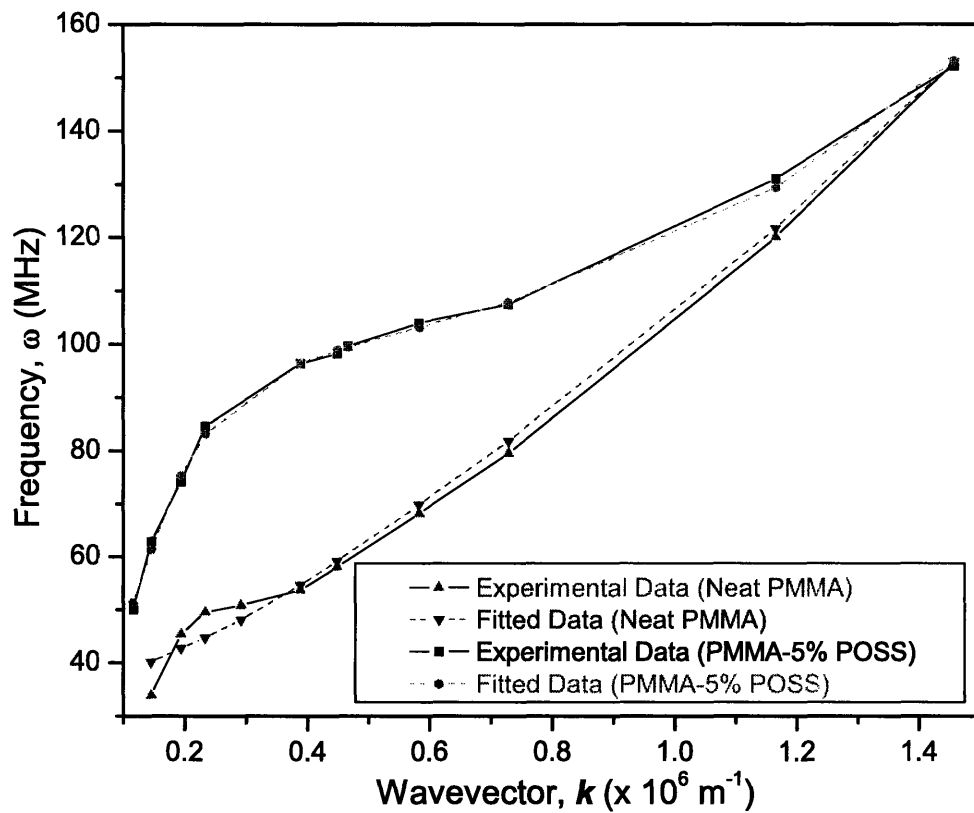
Figure 2-11: Acoustic dispersion relation showing frequency versus wavevector for neat PMMA and PMMA doped with 5 wt% methacryl-POSS for different acoustic wave vectors, along with theoretical calculations for a 1.1 μm thick polymer film.
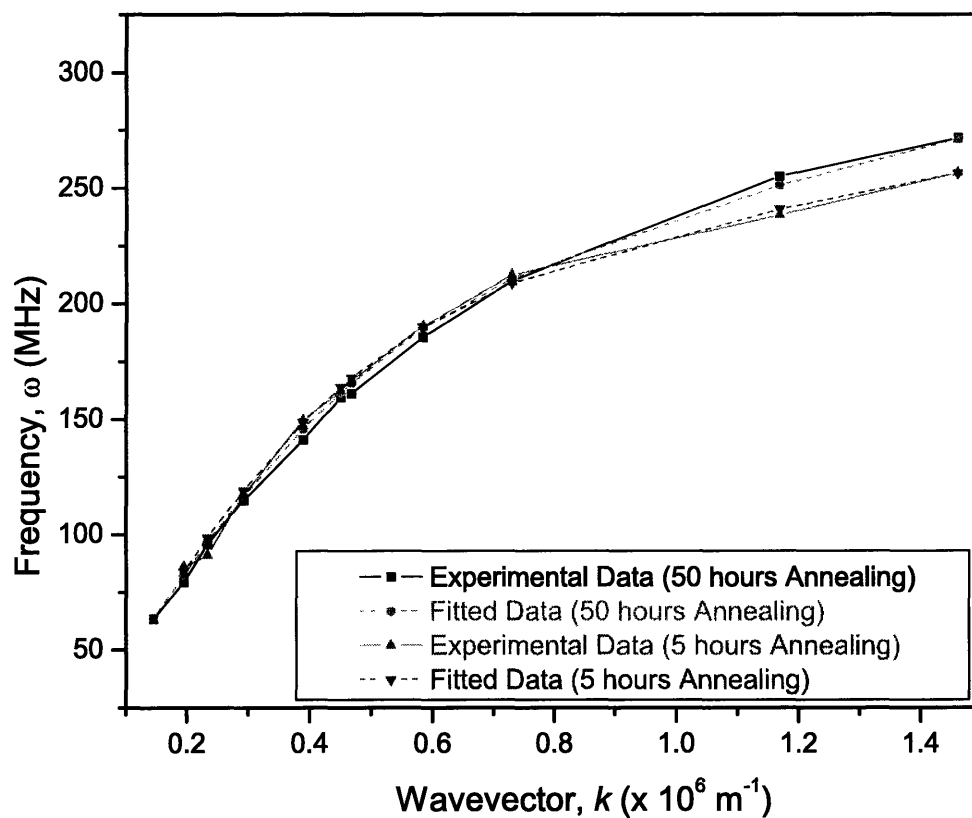
Figure 2-12: Acoustic dispersion relation showing frequency versus wavevector for PMMA-PI block copolymer as a function of annealing time, for different acoustic wave vectors, along with theoretical calculations for a 130 nm thick polymer film.
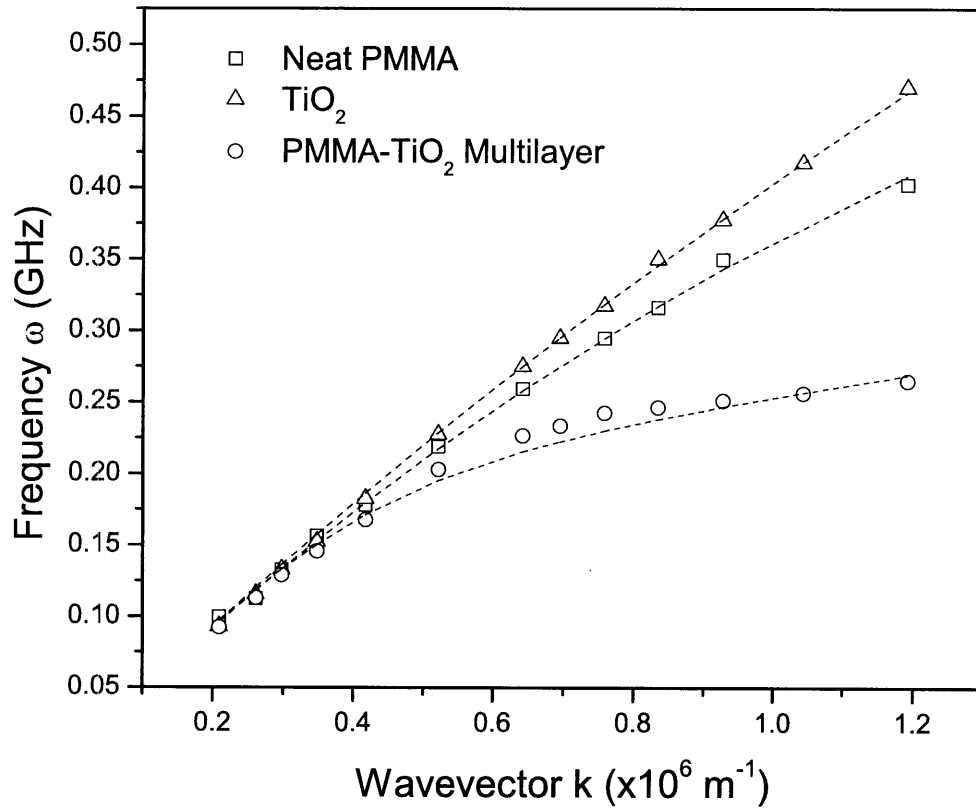
Figure 2-13: Lowest-order acoustic waveguide mode frequency dispersion curves of neat PMMA, neat TiO_2, and PMMA-TiO_2 multilayer structure. The dashed lines show numerical simulations through which dynamic mechanical parameters are determined.
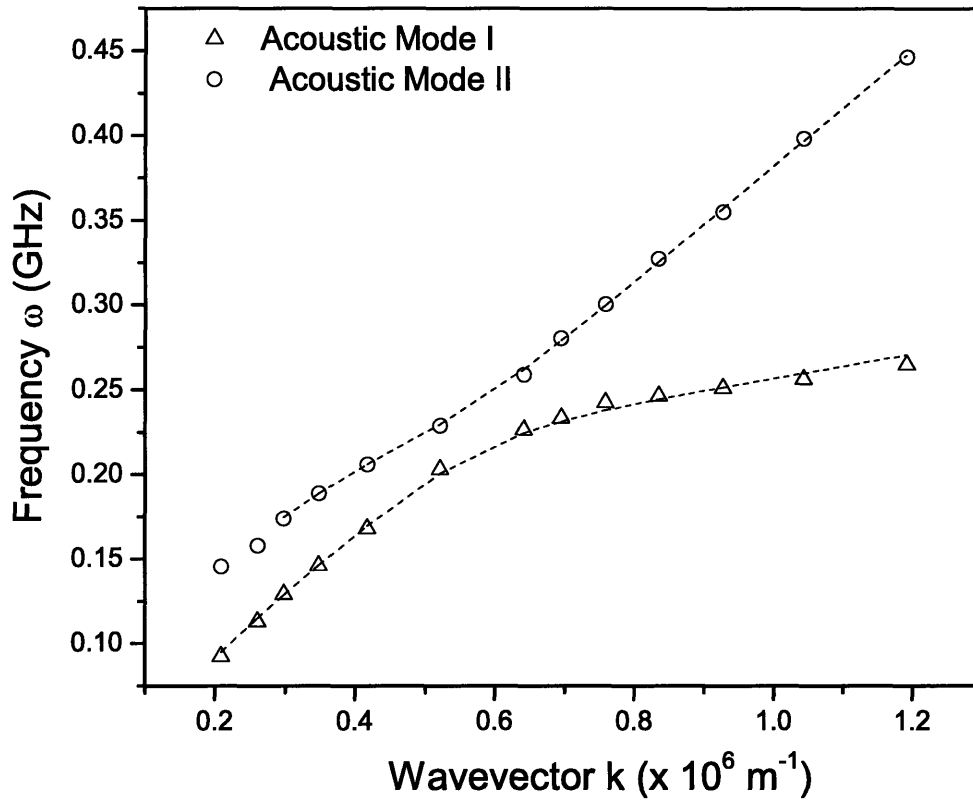
Figure 2-14: Acoustic waveguide mode frequency dispersion curves of PMMA-TiO$_2$ multilayer structure. The dashed lines show numerical simulations through which dynamic mechanical *effective* parameters for the multilayer structure are determined, assuming it was one uniform layer.

2.4 Results and Discussion

Results of ISTS characterization compare very closely to theoretical calculations based on the shear and bulk modulus values. The raw data measured yield the dispersion relation, $\omega(\vec{k})$. The analysis of this raw data is done by fitting the acoustic modes in the multilayer structure by iteratively varying parameters such as layer thicknesses, densities, and longitudinal and transverse acoustic velocities [14, 15]. Initially, thickness and density of the polymer film are fixed to roughly estimated value and the fitting is done varying the longitudinal and transverse velocities of the film. When the best fit is obtained, the thickness and density are also varied to see if this gives more closer fit or not. When the model fits the data well, a set of elastic constants including Young's modulus, shear modulus, bulk modulus, and Poisson's ratio can be calculated using Equations 2.6, 2.7, and 2.8. The results are tabulated in Table 2.1.

$$K = \rho \left(v_L^2 - \tfrac{4}{3} v_T^2 \right) \tag{2.6}$$

$$G = \rho \, v_T^2 \tag{2.7}$$

$$E = \frac{3\,K\,G}{K + \tfrac{1}{3}\,G} \tag{2.8}$$

where E=Young's modulus, K=bulk modulus, G=shear modulus, ρ=density, v_T= shear velocity, and v_L=longitudinal velocity.

We observe that the values obtained for elastic modulus of neat PMMA are different than the bulk literature values [30]. PMMA has density around 1.18 gm/cc and elastic modulus in the range 3.0–4.5 GPa, as determined by the bulk testing techniques. This is not surprising since the value of elastic modulus is highly sensitive to the method of film curing and hence the difference is probably due to intrinsic differences in sample characteristics. Also, the strain rate is higher (10^7 s^{-1}) in ISTS

Table 2.1: ISTS Data Analysis for PMMA–PI block copolymer and PMMA–POSS polymeric systems.

System	Longitudinal Velocity [km/s]	Transverse Velocity [km/s]	Density [g/cm^3]	Young's Modulus [GPa]	Shear Modulus [GPa]	Bulk Modulus [GPa]
Neat PMMA	2.3	1.4	1.1	5.4	2.2	3.1
PMMA–5 wt% POSS	1.2	1.3	1.1	4.4	1.8	2.6
PMMA–PI (5 Hours Annealing)	1.7	1.1	1.0	2.8	1.2	1.4
PMMA–PI (50 Hours Annealing)	2.1	1.3	1.1	4.1	1.7	2.6

measurements than standard mechanical testing techniques (0.001-0.1 s^{-1}), and the modulus goes up with increase in strain rate. The density of the PMMA-b-PI goes up with annealing since there is a decrease in free volume of glassy polymers like PMMA on heating. Hasan et al. demonstrated that the less aged material possesses higher free volume content below T_g than the annealed material [31].

Figure 2-15 shows dynamic mechanical analysis (DMA) performed on a TA Instruments Q800 DMA to measure the storage modulus of neat PMMA and 5 wt% POSS doped PMMA samples. As temperature is increased and PMMA goes through the β-transition, the storage modulus gradually decreases from 4.5 to 3.0 GPa. At the α-transition or glass transition, the storage modulus drops sharply from 2.5 GPa to 5.0 MPa. The glass transition temperature (T_g) of pure PMMA is 120 °C while 5 wt% methacryl–POSS doped PMMA has T_g close to 117 °C.

It can be seen that there is a slight decrease in the storage modulus of the doped sample compared to neat PMMA, which is in agreement with the bulk values determined through ISTS in Table 2.1. To the first approximation, we can simply take the storage modulus at a low frequency as the Young's modulus [32]. Figure 2-15 shows that the storage modulus (or Young's modulus) of neat PMMA is 3 GPa at room temperature while 5 wt% POSS doped PMMA has value close to 2.75 GPa. It has been mentioned that the incorporation of POSS in PMMA reduces monotoni-
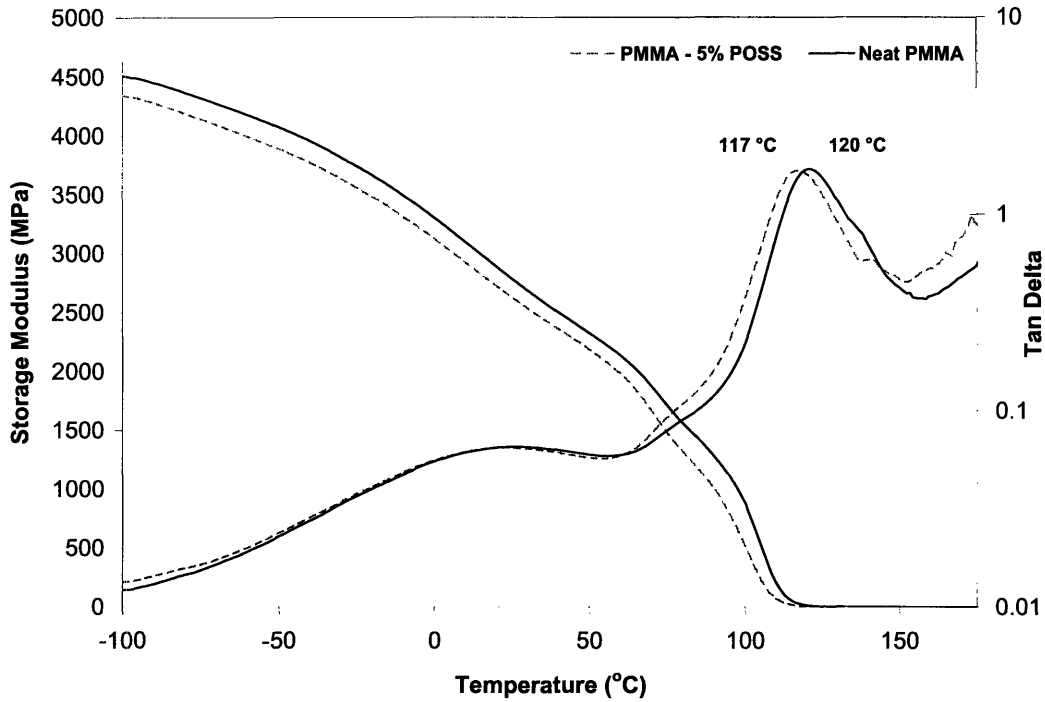
Figure 2-15: Dynamic Mechanical Analysis (DMA) data for PMMA–POSS system at 1 Hz done on TA Instruments Q800 DMA. Cylindrical polymer samples with a diameter of 2.8 mm and a length of 10.5 mm were tested in the cantilever mode in DMA with a fixed displacement of 25 μm. The testing temperature ranged from −100 to 180 °C with a 2 °C/min heating rate at frequency of 1 Hz, which was converted to corresponding average strain rate of 0.005 s^{-1}.

cally both the primary (α) and secondary (β) transition temperatures with increasing POSS content as studied by DMA [27, 33]. POSS enhances the mobility of the β-motions significantly and therefore reduces the resistance in high rate deformation. The bulkiness and quasi-spherical shape restrict POSS molecules from approaching the PMMA backbone [34, 35]. Thus, free volume increases in PMMA upon addition of POSS molecules and it acts as a *local plasticizer*.

Kopesky et al. investigated the toughness of PMMA using POSS nanocages and showed that molecularly dispersed methacryl–POSS leads to high toughness values [35] at quasi-static strain rates. This plasticization effect reduces the overall defor-

43

mation resistance of the polymer at low temperatures and high strain rates. By lowering the stress levels under these conditions, POSS may suppress certain brittle failure modes and increase the overall ductility of the polymer, thereby enhancing its energy absorption capabilities during impact [36]. The data in Table 2.1 agrees well with all these previous studies and shows a decrease of Young's modulus with methacryl–POSS doping.
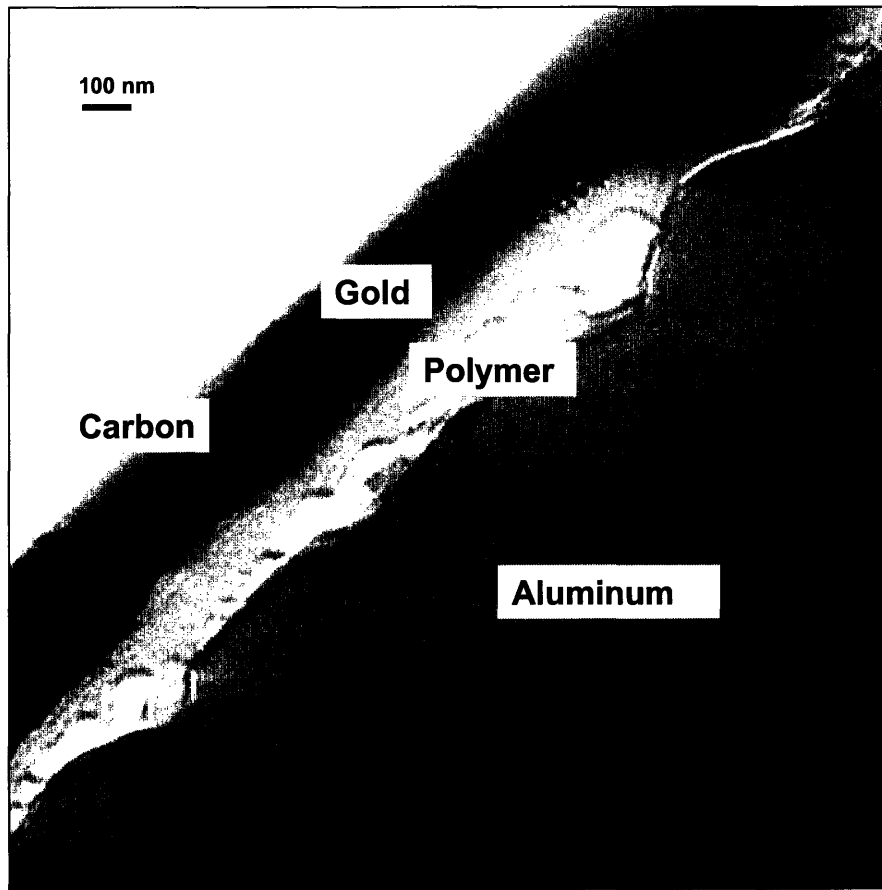
Figure 2-16: Transmission electron microscope (TEM) image for PMMA–PI block copolymer annealed for 50 hours. The scale bar is shown on the top left corner of the image and the cross-section of the sample assembly is schematically shown in Figure 2-5(a). The sample for TEM image was prepared by focused ion beam (FIB) so as to get neat cleavage of the cross-section and to keep the multilayer structure intact during imaging.

PMMA–PI block copolymer was further examined using transmission electron microscopy (TEM). The annealed copolymer should be microphase-ordered, exhibiting the lamellar morphology. However, this is not the case, as can be seen in Figure 2-16. Studies have shown that these copolymers confer a significant improvement in impact strength as annealing time is varied so as to let the lamellar morphology develop fully [37]. ISTS data in Table 2.1 show that the bulk modulus almost doubles with annealing time which is a significant improvement in the mechanical property of the material. The lamellar structure is not fully established after 2 days of annealing as can be seen in the TEM image. However, the annealed sample leads to higher stiffness that is reflected in higher acoustic frequencies and velocities. This may be due to partial ordering.

Thus, neat and polyhedral oligomeric silsesquioxane (POSS) doped poly(methyl methacrylate) (PMMA) samples were studied to examine the effects of composition on dynamic mechanical properties. ISTS data for PMMA-polyisoprene (PI) block copolymer thin films were also recorded. In this case, annealing enhances the periodic structural morphology of the copolymer, whose 13-nm lamellae are expected to show unique wavelength-dependent acoustic properties. The results illustrate the general value of ISTS measurements for revealing the effects of processing conditions on dynamic mechanical behavior.

There are many implications of this study. In particular, data were recorded from DMA at low frequency (1–100 Hz) and from ISTS at much higher frequency (10^9 Hz). Boyce et al. have investigated the rate-dependent deformation behavior of POSS–filled and plasticized poly(vinyl chloride) in intermediate frequency ranges close to 10^4 s^{-1} using split-Hopkinson bar technique [36, 27]. ISTS measurements as a function of temperature will permit the temperature–dependent relaxation dynamics to be assessed so the effects of processing, composition, etc. on dynamic mechanical

45

properties at the various frequency ranges could be compared. For example, if the microscopic motions are restricted or enabled by addition of POSS, would there be bigger effects at MHz or 1 Hz frequencies? At what temperature ranges would the effects be biggest at the different frequency ranges? How might the effects, discussed here in linear response, act as precursors for nonlinear responses including plastic deformation or flow? These are few of the questions which still need to be answered.

Figure 2-13 shows the dispersion curves of the neat PMMA, neat TiO_2, and PMMA-TiO_2 multilayer structure investigated. Numerical calculation of the lowest-order acoustic waveguide mode frequency dispersion curve was performed in order to extract the physical parameters of PMMA and TiO_2 that are indicated in Table 2.2. Averaged or effective properties for the multilayer structure, assuming it was one layer, were used for the PMMA-TiO_2 multilayer structure in Table 2.2. The outcomes of our fits are in good agreement with values for the bulk materials found in literature [21, 22]. Moreover, the dispersion curve of the multilayer structure PMMA-TiO_2 has been simulated quantitatively with the parameters extracted from the neat samples. The acoustic phase velocity values, which are lower than those of either constituent, are reproduced well. If we model the multilayer structure as a single equivalent layer, this layer has modulus values between those of PMMA and TiO_2 neat samples in this frequency range.

Figure 2-17 shows phase velocity dispersion curves for the neat PMMA, neat TiO_2, and PMMA-TiO_2 multilayer structure, along with limiting values for the substrate and the bulk materials. The qualitative trends are as expected, namely higher velocities, approaching that of the substrate, at shorter wavevectors in which the correspondingly longer acoustic wavelengths extend farther into the substrate and the acoustic wave more closely reflect the substrate properties. In each case, the shortest acoustic wavelengths are still longer than the film thickness d, i.e. we are always in

Table 2.2: Mechanical properties of neat PMMA, neat TiO_2, and PMMA-TiO_2 multilayer structure, extracted from the recorded acoustic dispersion curves shown in Figures 2-13 and 2-14 using ISTS technique. Effective values for the multilayer structure were calculated assuming it was a single uniform layer.

Material System	Density [g/cm^3]	Young's Modulus [GPa]	Bulk Modulus [GPa]	Shear Modulus [GPa]	Poisson's Ratio
Neat PMMA	1.1	4.9	4.3	1.9	0.3
TiO_2	3.6	210	154	83	0.3
PMMA-TiO_2 (Multilayer Structure)	2.2	12	12	4.7	0.3
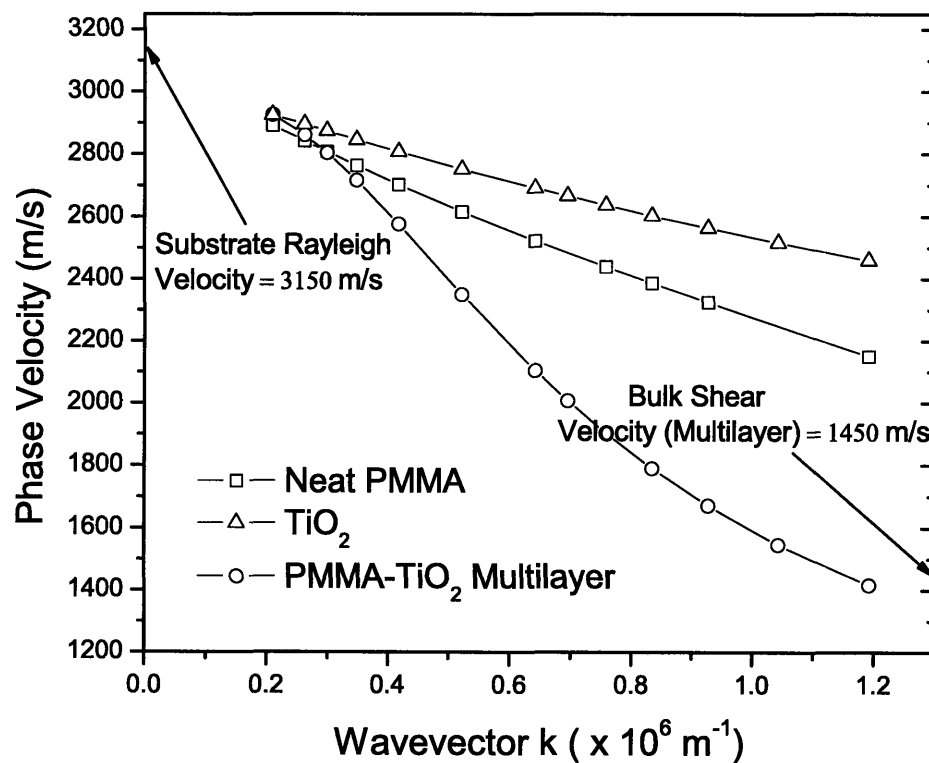
Figure 2-17: Acoustic phase velocity dispersion curves of neat PMMA, neat TiO_2, and PMMA-TiO_2 multilayer structure.

47
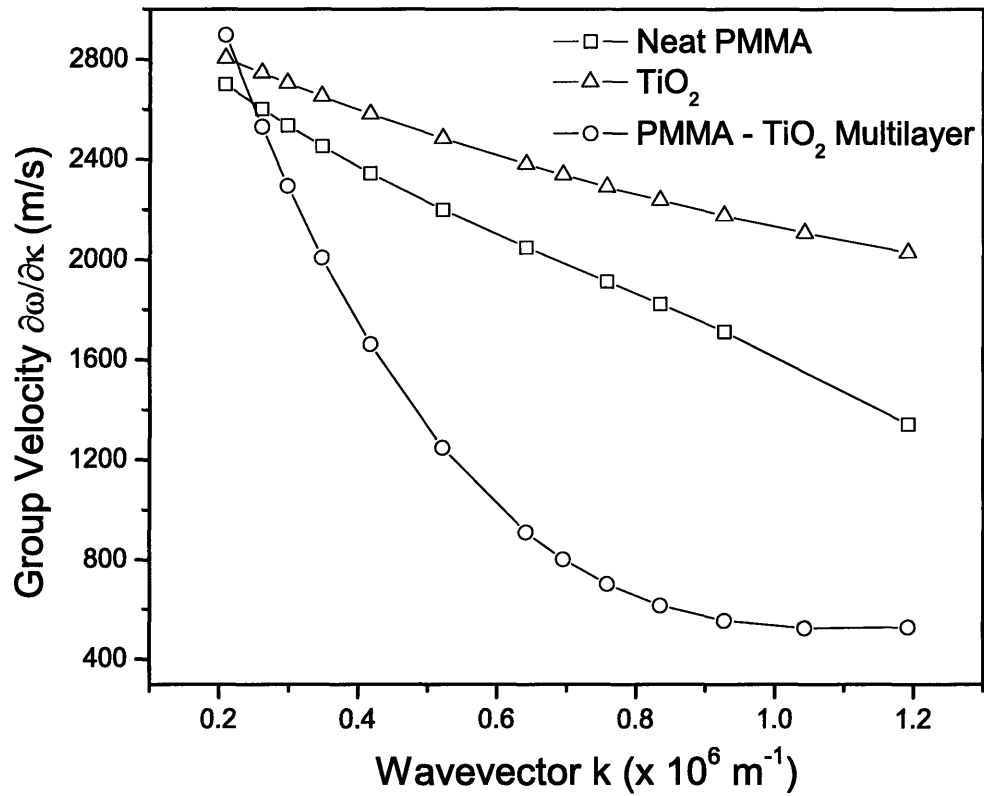
Figure 2-18: Acoustic group velocity dispersion curves of neat PMMA, neat TiO$_2$, and PMMA-TiO$_2$ multilayer structure. Note the very low group velocity of the multilayer structure in the high-wavevector range. There is strong dispersion in the group velocity at higher frequencies. This is useful since it breaks a short acoustic wavepacket like an incipient shock wave and thus could help prevent shock formation.

the kd≪1 regime and so the bulk values that would be reached in the limit of very short wavelength are never approached closely, but the trend is toward these values as wavevector is increased.

Figure 2-18 shows the group velocity dispersion curves for the neat PMMA, neat TiO_2, and PMMA-TiO_2 multilayer structure. Of particular interest is the result for the multilayer sample, in which the group velocity is extremely low in the range of higher acoustic wavevectors. This means that the speed of acoustic energy transport in the plane of the multilayer film is unusually slow at these wavevectors. This may have useful implications for dissipative structures since slow speeds offer longer times for damping to occur. In this structure, the low group velocity appears to arise from an avoided crossing between the two lowest order acoustic waveguide modes. More generally, acoustic bandgap structures might be constructed that would exhibit similar properties in all directions in selected wavevector ranges.

Thus, ISTS measurements have been made on a PMMA-TiO_2 multilayer structure that may serve as a prototype for acoustic bandgap materials or other designs with substantial acoustic impedance mismatch between alternating layers. The lowest-order acoustic waveguide modes have been characterized in samples composed of the individual materials and in the multilayer structure in the sub-GHz frequency range. Throughout this range, the acoustic phase velocities in the multilayer sample are lower than those of either of the two components and the modulus values of the multilayer structure lie between those of the components. A regime has been observed in which the multilayer structure exhibits extremely low acoustic group velocity in the lowest-order waveguide mode, suggesting possible applications in structures that exploit the slow sound speed for increased dissipation or, at larger amplitudes, improved mitigation of dynamic mechanical impact.

49

Chapter 3

Shock Waves

3.1 Introduction

A shock is a sudden or violent disturbance in the equilibrium of a system. In other words, it is a discontinuity in pressure, temperature (or internal energy), and density. Shock can result from impact: drop shock, ballistic shock, and automotive crashes or from explosives in the case of pyroshock and blasts. An excellent review on the fundamentals of stress wave phenomena is given by D. B. Hayes [38]. Shock waves are high-speed, large-amplitude mechanical transients generated by violent impacts or explosions. In this chapter, the basic principles of shock waves are reviewed and interferometric characterization of shock waves is discussed.

A shock pulse travels through a material at a speed (U_s) equal to the sum of the particle velocity (U_p) and the medium's acoustic velocity (c): $U_s \approx U_p + c$. The particle velocity is the speed with which the material at the point of interest is moving, the velocity of material flow behind the shock front. Accordingly, the shocked region exhibits higher density than unshocked regions. Hayes states that the cause of a shock is a material's property of transmitting sound faster with increasing pressure (density)
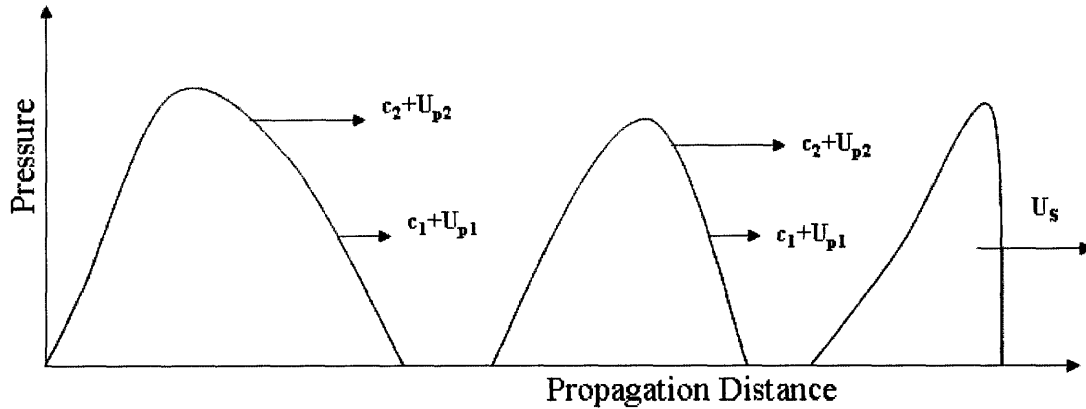
Figure 3-1: Schematic showing the formation of a shock wave. As the disturbance propagates from left to right, the front becomes increasingly steep, until it becomes instantaneous. This implies a discontinuous jump in pressure (and correspondingly, density), as shown to the right. U_s is the shock velocity, U_p is the material velocity and c is the acoustic velocity. Typically, $U_s \sim$ several km/s or nm/ps (Hayes, 1976 [38]).

[38]. The fundamental requirement for the establishment of a shock wave is that the velocity of the pulse (U_s), increases with increasing pressure (P). As shown in Figure 3-1, a high-pressure trailing shock edge will steepen because higher-pressure shocks travel faster. Thus a compressional wave will continue to propagate faster until its front exhibits a discontinuous jump in pressure – the formation of a shock.

Typical blast shock velocities are in the range of 4–9 km/s [39]. The intense compression, the shock induces is followed by recoil or rarefaction, which is rapid expansion of the material. Just as conventional high-rate testing techniques (*e.g.* split–Hopkinson pressure bar and gas gun testing), laser-induced shock loading is a thermodynamically irreversible adiabatic process because the compression is nearly instantaneous, accompanied by an entropy increase [40]. However, multiple-stage shock compression, known as shock ring-up, follows an isentrope curve and is a reversible process. Compression can be up to 20% in some cases, with an associated temperature rise of hundreds of degrees – all within tens of picoseconds. After the

Table 3.1: Typical values of strain rates observed under various conditions.

Method	Strain Rate $[s^{-1}]$
Instron	10^{-1}
Drop-weight	10^2
Split–Hopkinson pressure bar	10^2–10^4
Blast/Explosion	10^5
Gas gun/Bullet/Flyer Plate	10^5–10^6
Laser–induced shock	10^8

shock passes, cooling occurs at a fantastic rate of few hundred billion degrees per second in the case of single-stage shock compression [41, 39].

The primary methods of shock generation are mechanical or projectile-impact shock loading and laser-induced shock loading [42]. The two realms of shock loading are similar in principle since laser shocking drives a thin film of aluminum serving as a battery ram. The major difference between the two approaches is the duration of the shock pulse. Laser–initiated shocks usually do not last longer than several nanoseconds, whereas mechanical shocking leaves the sample in a constant pressure steady state for microseconds. Because the ensuing stress states last for different lengths of time in laser-induced and gas gun shocking, the timescale over which material behavior is probed is different [43].

A pressure-volume (P-V) diagram is directly measured during a shock experiment. A typical P-V compression curve is shown in Figure 3-2, along with the thermodynamic path for a shock. Note that the shock Hugoniot is defined as the curve (locus) which depicts available shock states. Figure 3-3 shows the shock loading and unloading curves.

The quantitative relationship which governs the behavior of shock waves is derived by using the Rankine-Hugoniot equations. Given 1–D steady flow of a compressible,
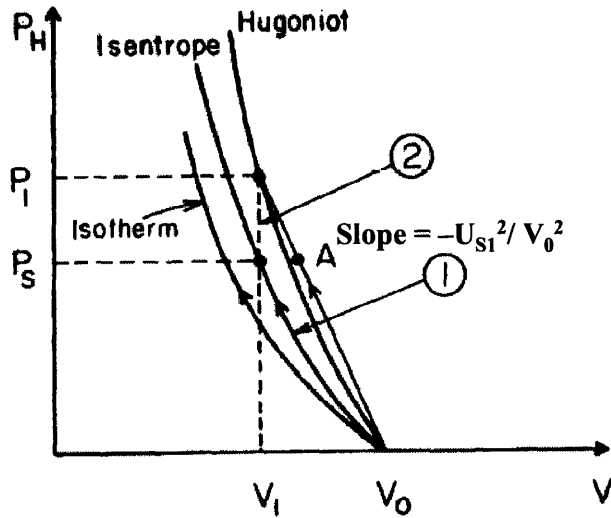
Figure 3-2: Pressure-volume compression curves. For isentrope and isotherm, the thermodynamic path coincides with the locus of states. For shock, the thermodynamic path is a straight line to point (P_1, V_1) on the Hugoniot curve, which is the locus of shock states (Ahrens, 1995 [44]). $V_0 = \frac{1}{\rho_0}$ and $V_1 = \frac{1}{\rho_1}$.
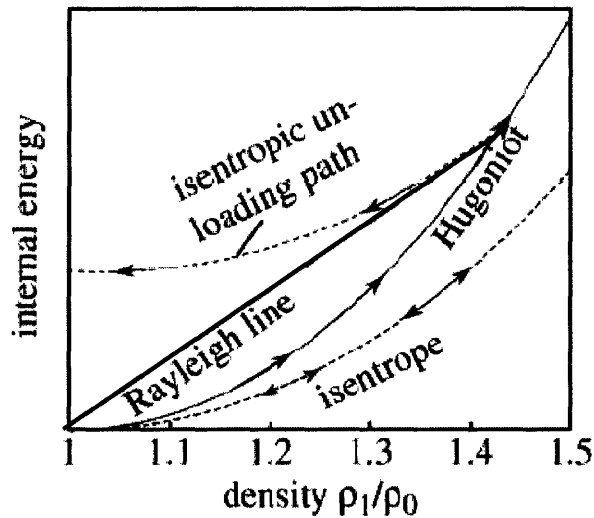
Figure 3-3: Shock loading and unloading curve. ρ_0 and ρ_1 are the densities of unshocked and shocked material respectively. The shock (irreversible) compression follows a Rayleigh line to the Hugoniot and shock unloading is always isentropic [41].

inviscid (non-viscous) fluid, the following equivalent expressions of conservation of mass, momentum, and energy all apply:

$$\rho_1 = \rho_0 \left(1 - \frac{U_p}{U_s}\right)^{-1} \tag{3.1}$$

$$P_1 - P_0 = \rho_0\, U_s\, U_p \tag{3.2}$$

$$E_1 - E_0 = \tfrac{1}{2}(P_1 + P_0)\left(\frac{1}{\rho_0} - \frac{1}{\rho_1}\right) \tag{3.3}$$

where ρ is density, U is speed, P is pressure, E is internal energy per unit mass, and the subscripts 0 and 1 indicate initial (unshocked) and final (shocked) conditions, respectively. In the above conservation equations (3.1)–(3.3), there are five variables: pressure (P_1), particle velocity (U_p), shock velocity (U_s), density (ρ_1), and energy (E_1). Hence, an additional equation is needed if we want to determine all parameters as a function of one of them. This equation can be expressed as the relationship between shock and particle velocities, and has to be experimentally determined.

$$U_s = c + S_1\, U_p \tag{3.4}$$

where c is the acoustic velocity in the material at zero pressure and S_1 is an empirical parameter. For most materials not undergoing phase transitions, Equation (3.4) is valid and a linear relationship describes fairly well the shock response of materials. The free-surface velocity, U_{fs}, is twice the particle velocity of the shock pulse, U_p, and can be determined by laser interferometry. This allows determination of all other shock parameters.

3.2 Shock Characterization

Shock waves in solids are characterized by a sharp discontinuity in the thermodynamic variables of the material. Shocks are generated using explosive charges, gas-driven projectiles, or high-energy laser sources. The repetition rate is high, and the cost per shock is low, in case of laser-induced shock. A well-characterized shock is desired, with a steeply rising planar shock front running at a constant velocity. Ultrafast time-resolved interferometry has been used to measure shock wave breakout and is a powerful means of investigating shock dynamics in a variety of materials. It provides detailed information about the dynamic optical properties and pressure profile of laser-generated shocks propagating in materials [45, 46, 47, 48, 49].

Typically, a shock wave propagating through a material at a velocity of ~6 km/s causes particles in the material to jump to a velocity of 1 or 2 km/s. Interferometric data have been well-modeled using bulk Hugoniots, and the use of direct laser drive does not lead to a thermodynamic state significantly from the Hugoniot, allowing us to make the assumption that on these timescales (hundreds of picoseconds), the states are well-approximated as the same states obtained with gas-gun systems [50].

The time profile of the shock breakout event is built up from many repeated single shot interferometry measurements on different nearby sample regions, over a range of time delays between the shock generating pulse and the probe pulses. Two types of femtosecond time-resolved interferometry are used to characterize the shock. Both utilize a modified Mach-Zehnder interferometer with the sample in one arm and a time delay in the reference arm. In contrast to shock experiments with gas guns in which obtaining synchronicity to a few picoseconds is extremely difficult and time-resolution is provided by fast streak cameras, optical synchronicity is simply obtained by changing the optical path lengths with translation stages and the time resolution

56
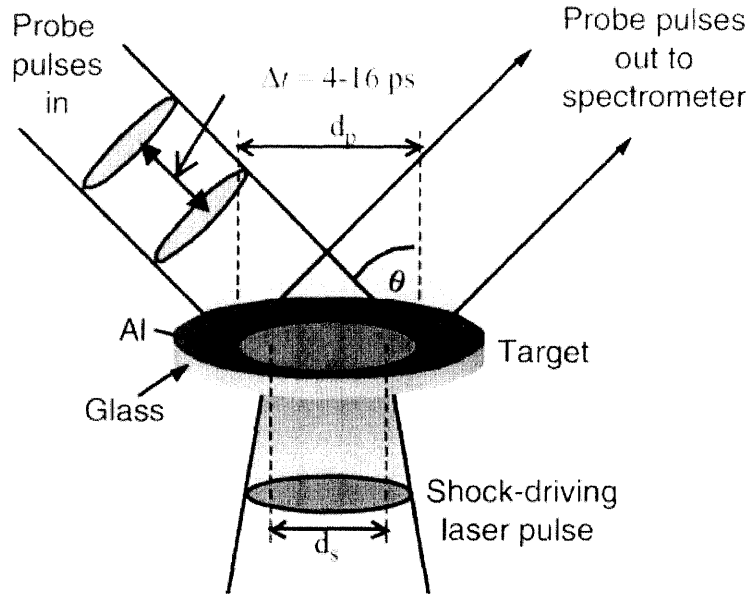
Figure 3-4: Schematic diagram of the femtosecond laser-driven shock frequency domain interferometric experiment [50].

results from the pulse duration (130 fs in our case) which gives the duration of the frames that are recorded as a function of delay.

In spectral interferometry or frequency domain interferometry, the reference arm is slightly longer than the sample arm and the beams are recombined collinearly and focused into a spectrometer. The two probe pulses are stretched in time by the spectrograph, so that they overlap in time and space at the CCD and produce an interference pattern along the wavelength axis. The resulting CCD image for each experiment is analyzed using Fourier transform methods to extract the difference in phase between the two probe pulses caused by changes in the film surface position or the optical properties of the metal [51]. The experimental arrangement is shown schematically in Figure 3-4.

Geindre et al. determined the relative phase shift between the probe pulses caused by motion of the free surface and/or transient changes in the optical properties of
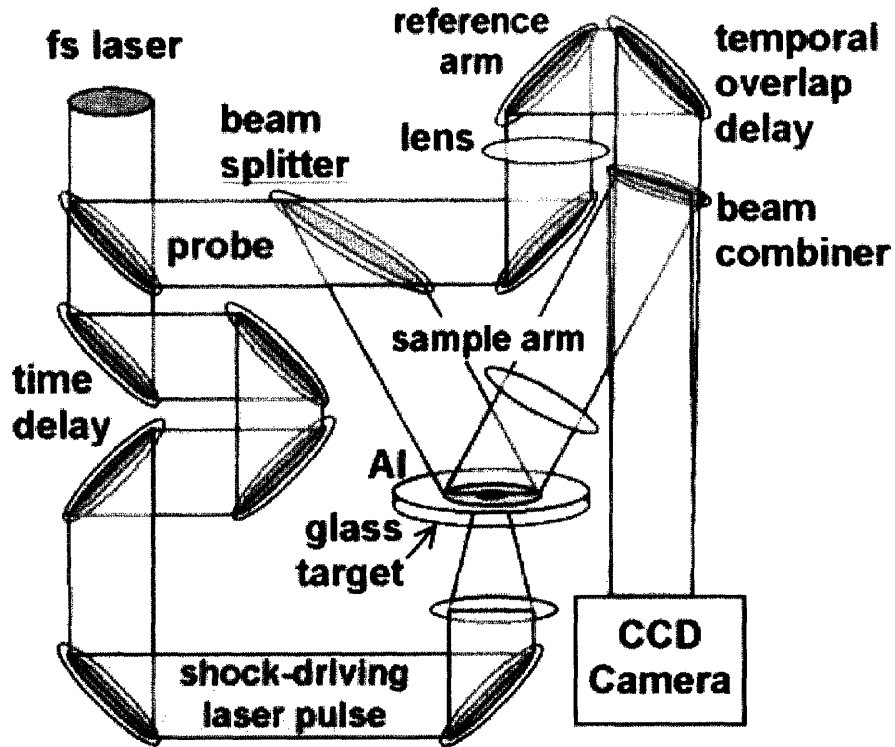
Figure 3-5: Schematic diagram of the femtosecond laser-driven shock spatial interferometric experiment [46].

the surface during shock breakout, by performing an inverse fast-Fourier transform on the spectral intensity interferogram recorded on the spectrograph CCD [52]. If the shock arrives at the metal surface after both probe pulses, the surface is essentially unchanged, giving zero phase shift. If the shock arrives between the two probe pulses, the measured phase shift is proportional to the fraction of the time between probe pulses that the surface is moving. If the shock arrives before both probe pulses, a maximum phase shift is reached [53].

In femtosecond time-resolved two-dimensional spatial interferometry, the reference and sample arms of the interferometer are made the same length to adjust the temporal overlap between the two arms and maximize fringe contrast and the beams are combined non-collinearly, so that an interference pattern is produced at the CCD (no

spectrograph is used). Two dimensional spatial information about material motion and/or sample optical properties is obtained from the interference patterns using 2-D Fourier transform methods [54]. Two different angles of incidence of the sample beam are used to extract the relative contributions of the two effects.

Gahagan, Funk and Moore have demonstrated 2-D spatial interferometry [55, 56], using thin aluminum and nickel films (250 nm to 2 μm nominal thickness) that were vapor plated onto borosilicate microscope slide cover slips (150 $\pm$ 20 μm thickness) as target samples. A single 800 nm, 130 fs FWHM, 0.7 mJ laser pulse generated by a seeded, chirped pulse amplified Ti:sapphire laser system was used for both shock generation and probing. The shock generating pulse (0.2–0.5 mJ) was focused through the glass substrate onto the glass/metal interface to a spot size of 75 mm. The shock wave produced in this manner has been shown to have a nearly planar spatial profile instead of Gaussian due to optical limiting and self-focusing Kerr effect in the substrate [57]. The experimental arrangement is shown schematically in Figure 3-5.

The final pressure achieved in the aluminum was determined from the corresponding shock and particle velocities in the bulk film derived from the free surface velocity measurements. The slopes of phase shift versus time, $\Delta\phi/\Delta t$, in Figure 3-6 determine the free surface velocity U_{fs}, and the aluminum particle velocity U_p in the bulk material was $\approx U_{fs}/2$. The shock speed U_s and pressure P in the initially unshocked aluminum can be determined from the particle velocity, the aluminum Hugoniot (experimental U_s versus U_p relation), and the Hugoniot–Rankine equations that account for conservation of mass, energy, and momentum across a shock discontinuity [58, 59]. For aluminum, $U_s = 1.34\,U_p + c$, where c = 5.35 nm/ps, and the longitudinal sound speed is 6.38 km/s [60]. Pressures were calculated using the relation $P = U_p\,U_s\,\rho$, where ρ is the density of unshocked aluminum, 2.712 g/cm^3.

Interferometric results as a function of shock strength suggest that sub-micron
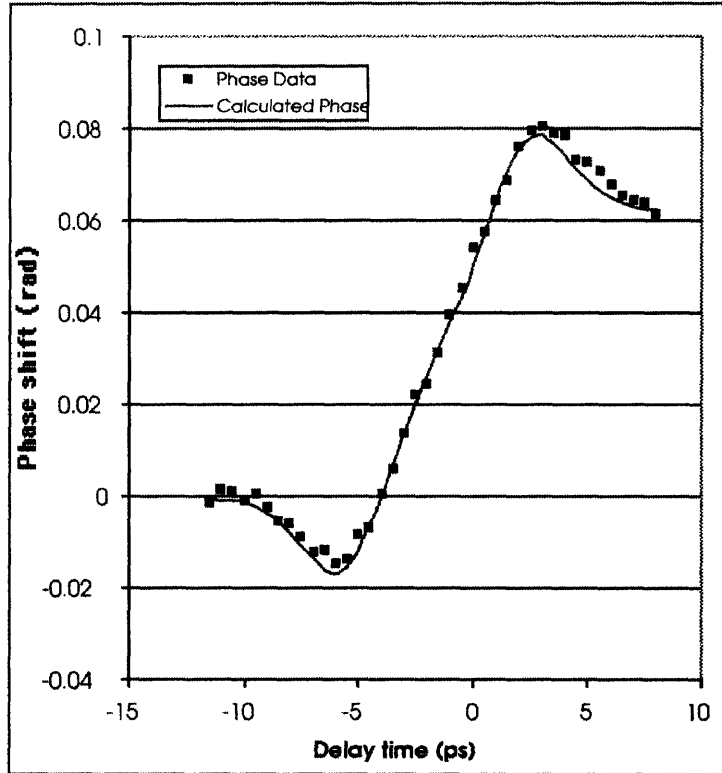
Figure 3-6: Phase shift measured by spectral interferometry as the shock wave exits the free surface of a 750 nm thick Al layer on borosilicate glass substrate. Probe was 800 nm, and the angle of incidence was 32.6° [51]. The large negative phase shift is associated with the pressure dependence of the interband transition in Al.

films have essentially the same material response to shock loading as macroscopic samples [61, 62] and the Hugoniot (locus of final states reachable in a single shock) of the thin film material is indistinguishable from that of bulk material. The similarity of the thin film and bulk Hugoniots supports the use of thin film shock dynamics measurements, which allow the temporal and spatial resolution necessary to characterize molecular properties, to contribute to a detailed understanding of larger-scale shock phenomena [54]. Thus, we have shown that interferometric techniques allow characterization of laser driven shocks.

Chapter 4

Shock Wave Spectroscopy

4.1 Introduction

There are various spectroscopies being used as probes of material response to shock. The time resolution in most time-resolved spectroscopy is limited by the optical instrumentation, either the pulse or the detector. In shock wave spectroscopy, time resolution is limited by the instrumentation as well as the time needed for the shock to traverse the part of the sample that is monitored by the probe pulse, which depends on many parameters including the probe absorption strength. In this chapter, several types of time-resolved spectroscopy of shocks are reviewed for possible background and context for our own measurements. Preliminary ISTS measurements of samples are presented to demonstrate that we can probe materials on single shot basis under shock loading.

4.2 Previous Studies

This section reviews work done on generating shock by various techniques as well as different kinds of tools being used for shock measurement. It presents studies done using a gas gun to generate shock on one hand and laser-induced shock loading on the other. Also, different measurement techniques of probing material under shock loading like Raman scattering, coherent anti-Stokes Raman scattering (CARS) and ISTS have been discussed.

4.2.1 Gas Gun Spectroscopy

Gupta has studied the impact response of polymers such as polymethyl methacrylate (PMMA) under gas gun loading, measuring parameters similar to those in ISTS measurements. Large amplitude one-dimensional compression and shear wave measurements were made and shear and longitudinal wave velocities were used to determine the shear modulus, bulk modulus, and the mean stress-volume relations under impact loading using wave velocity analysis. He reports longitudinal particle velocities and compressional and shear wave velocities on the microsecond timescale as shown in Table 4.1. Clearly, there is an increased wave propagation speed and transient density compared to the acoustically measured value of 2.83 km/s for unshocked PMMA [18]. These extremely difficult measurements have not been repeated on any material since this 1981 study.

4.2.2 Laser Shock Spectroscopy

There are several research groups that have investigated polymeric materials under laser-induced shock-loading with different experimental techniques. In principle any linear, nonlinear, or coherent optical technique performed using the laser can be used

Table 4.1: Experimental values for PMMA under gas gun shock loading [63].

Longitudinal Particle Velocity [km/s]	ρ_1/ρ_0	$c_{\text{compression}}$ [km/s]	c_{shear} [km/s]
0	1.0	2.83	1.10
0.13	1.04	3.31	1.48
0.18	1.06	3.40	1.51
0.22	1.07	3.45	1.52
0.27	1.09	3.61	1.51

to probe the shocked sample. The time resolution of the technique is ultimately limited by the sample thickness.

The problems associated with probing shock fronts are that shock waves moving at a velocity of a few nm/ps are very slow compared to light moving a few hundred μm/ps. If one wishes to probe only molecules within a few ps of the shock front, then ideally a quite *high spatial resolution* of a few tens of nanometers is needed. This spatial resolution cannot be achieved merely by focusing laser pulses tightly because it is much smaller than a wavelength of visible light. Instead, we have to use a sample of nanometer thickness. The problem with a very thin layer is getting ultrafast spectra with good signal-to-noise [64].

Nanosecond time-resolved Raman spectroscopy is used to investigate structure and bond strength of molecules and crystals under shock compression using pump and probe technique [65]. Polytetrafluoroethylene (PTFE), was studied under laser-driven shock compression at 2.3 GPa (laser power density of 4.0 GW/cm^2). A new vibrational line at 1900 cm^{-1} appeared only under shock compression and was assigned to the C=C stretching in transient species produced by the shock-induced bond scission.

Time-resolved Raman spectroscopy studies were performed on benzene derivatives under laser-driven shock compression up to a few GPa using a pump-probe technique,

in order to investigate the effect of steric and chemical structures on molecular dynamics of shock compression [66]. Under shock compression at 1.3 GPa, the ring-breathing mode of benzene showed a high frequency shift of 10 cm^{-1} which corresponded to a ring reduction of 0.7%. The magnitude of the frequency shift showed a systematic dependence on intermolecular distance; the ring-breathing mode is decreased, while the ring-vibrational is increased, as molecules are forced to come close together.

Dlott et al. use coherent anti-Stokes Raman scattering (CARS) as a probe [41, 67, 68, 69]. CARS is a form of time-resolved nonlinear vibrational spectroscopy in which a pair of optical fields drives a coherent vibrational response. It is a multiphoton process whereby lasers with two different pump frequencies, ω_1 and ω_2, are used to excite a specific vibrational resonance at the difference frequency, $\omega_0 = \omega_1 - \omega_2$. Coherent anti-Stokes Raman scattering of a variably delayed probe pulse of frequency, ω_3, (which may be the same as either pump frequency) yields signal at a unique frequency, $\omega_3 + \omega_0$, which is spectrally isolated and detected. Shock-induced changes in the selected vibrational frequency can be measured as a function of time.

CARS probes chemical bonds on ultrafast time scales but to observe shock-induced effects with femtosecond time resolution, an extremely thin layer must be monitored since if the probe light sees a thick region then it sees material shocked at very different times. Dlott resolves this by considering just one monolayer of the molecules being studied, so even though the CARS light beams scans a lot of material, only that layer produces signal with the molecular vibrational frequency that is being measured.

The nanoshock technique developed by the Dlott group is depicted in Figure 4-1. CARS was used as a probing technique and laser pulses (150 μJ, 80 ps and 100 μm spot size) were used for shock generation. Figure 4-2 shows polycrystalline anthracene CARS spectra near 1400 cm^{-1} before and after shock. A microfabricated shock target array assembly is used, consisting of a polymer shock generation layer,
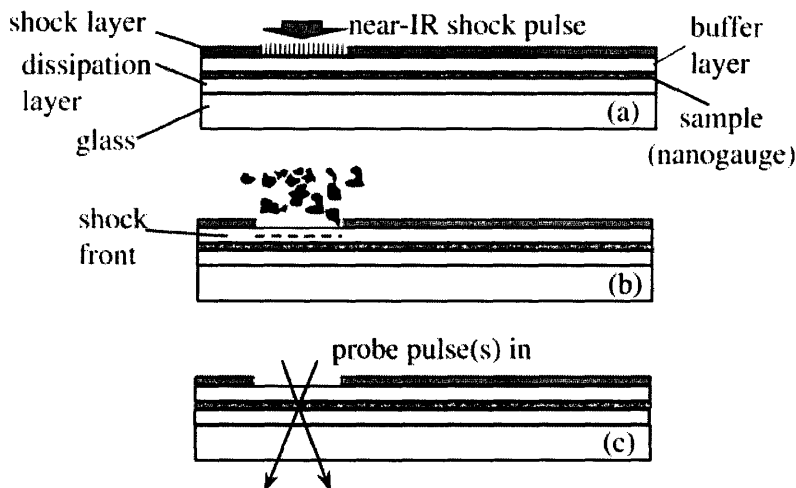
Figure 4-1: Schematic of the Nanoshock technique [41, 68]. (a) A near-infrared (IR) pulse ablates the shock layer, consisting of a near-IR dye and a decomposable polymer, (b) launching a shock into the nanometer-thickness sample layer (optical nanogauge). (c) After the shock layer has ablated, time-delayed pulses probe the sample layer.

a polymer buffer layer, and a thin sample layer (optical nanogauge).

The CARS spectra in Figure 4-2 shows that the Raman transition blue–shifts about 16 cm^{-1} and almost doubles in width. The shift is mainly a function of density (or pressure) and the width is a function of temperature.

Figure 4-3 shows the CARS spectra with evolution of time. The shock is initiated and it enters the anthracene layer at $t \approx 1.45$ ns and exits at $t \approx 1.63$ ns with a velocity of 4 km/s. The remarkable feature is that two distinct spectral transitions are observed when the shock front is inside the layer. As the shock front progresses through the sample layer, the intensity of the ambient peak declines and while that of shocked peak increases.

Figure 4-4 shows CARS spectra during shock unloading, which is always a reversible process and the pressure in the anthracene layer is everywhere equal to the external pressure, so there is only a single peak in the spectrum, which red-shifts and narrows in a few nanoseconds. The red-shifting indicates pressure release and the
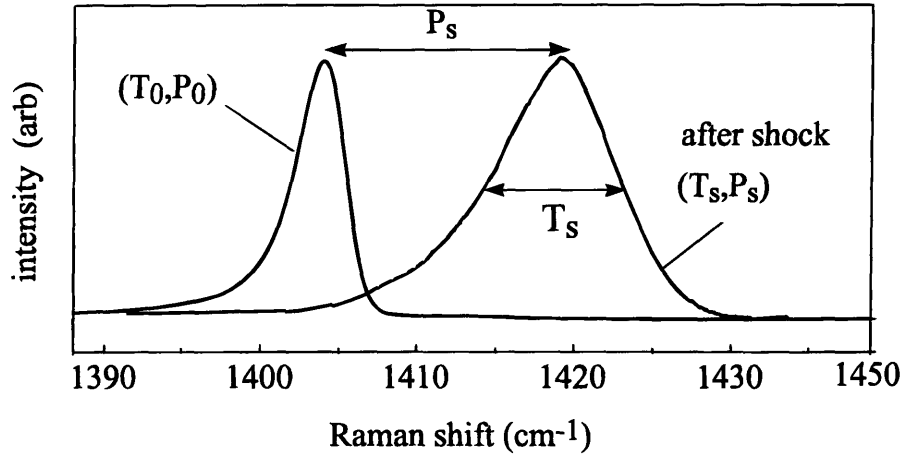
Figure 4-2: Coherent Anti-Stokes Raman (CARS) spectrum of a 700-nm layer of polycrystalline anthracene in a shock target array near 1400 cm^{-1} transition [64, 68]. The frequency shift can be used to estimate the shock pressure P_s. The spectral width can be used to estimate the shock temperature T_s. Here, $P_s \approx 4.2$ GPa and $T_s \approx 350\,°C$.

narrowing indicates cooling [70].

Thus, the nanoshock can be viewed as a sudden ultrafast uniaxial compression which is fast enough to generate non-equilibrium mechanical states and which involves a sudden jump to high temperature and pressure. It is a fast shock pulse, where the material is suddenly compressed and then more gradually expanded.

Tas et al. have also characterized the nanoshock waveform by measuring the shock front rise-time, shock fall-time, peak pressure, and velocity using CARS [71, 72]. Lagutchev et al. have used laser-driven ~1 GPa shock waves to dynamically compress self-assembled monolayers (SAMs) [73]. They have shown evidences of a complicated viscoelastic response of the materials under shock loading and that the SAM response to shock is dependent on both the molecular structure and on the lattice structure as determined by the metal substrate. In viscoelastic shock compression the shock front consists of two parts, a faster elastic part and a slower plastic deformation part. As

Figure 4-3: Time evolution of CARS spectra of a 700-nm layer of polycrystalline anthracene during shock loading [41]. Two distinct spectral transitions are observed when the shock front is in the middle of the layer, corresponding to ambient and shocked anthracene.
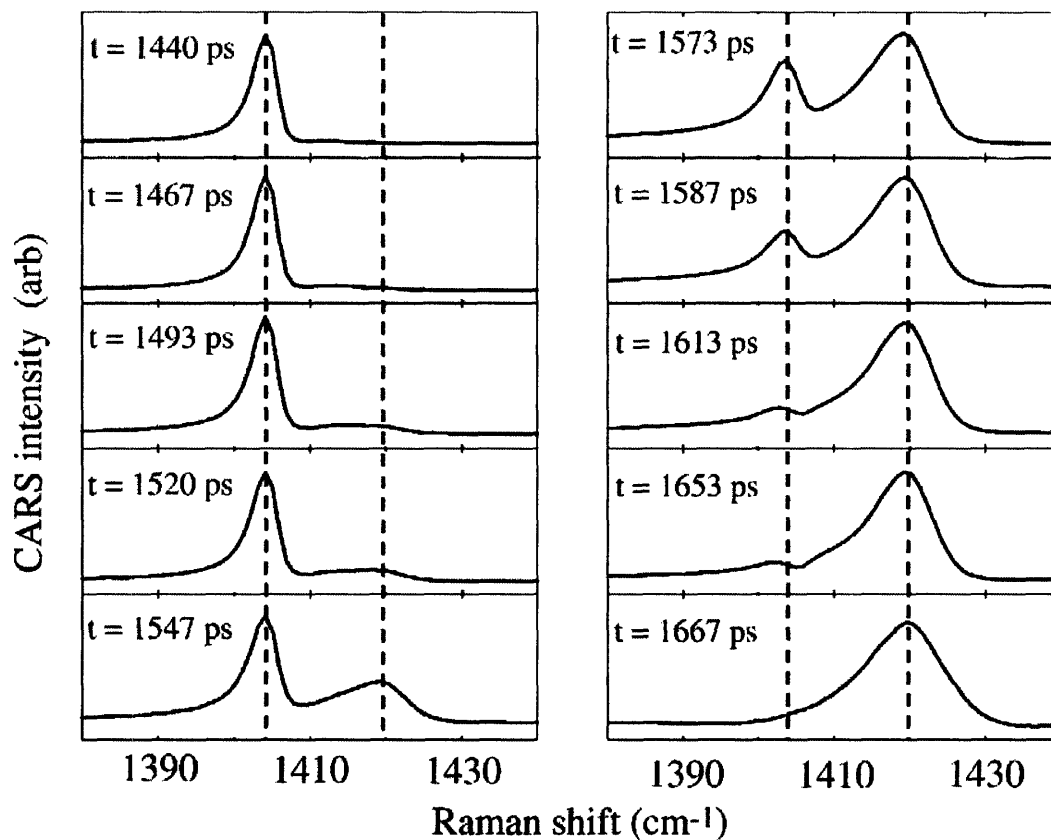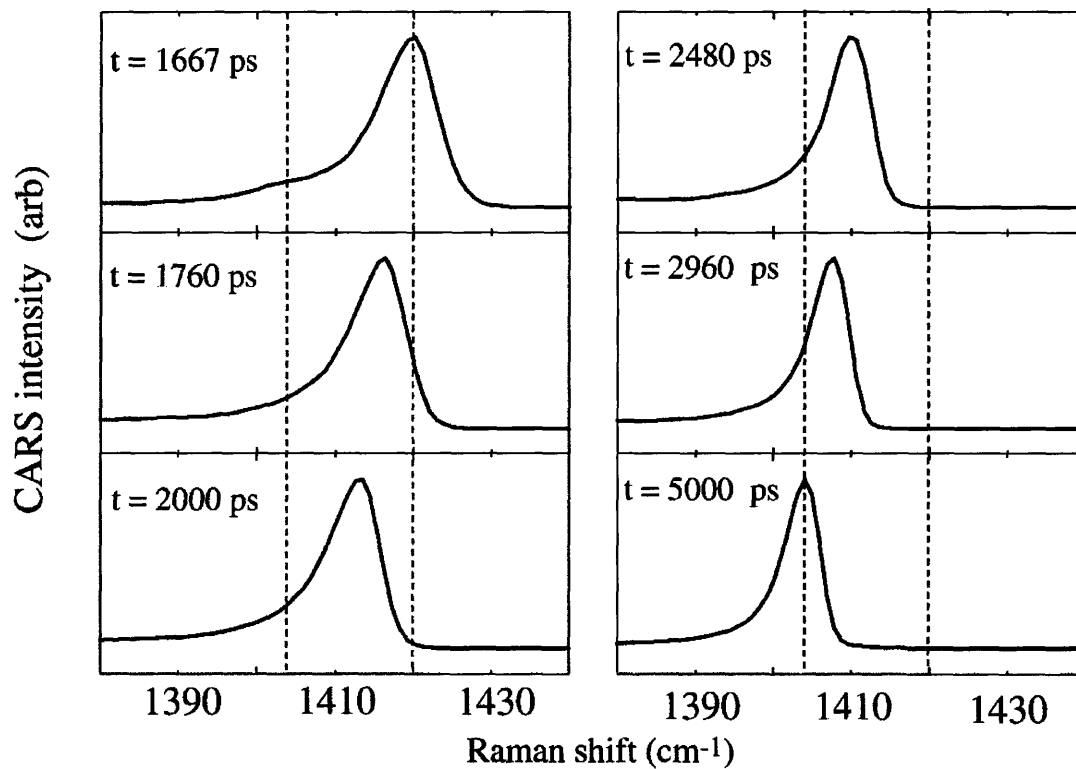
67

Figure 4-4: Time evolution of CARS spectra of a 700-nm layer of polycrystalline anthracene during shock unloading [41].

the front propagates, the elastic part moves ahead and disperses whereas the plastic part lags behind and remains steep which is a measure of the rate of mechanical deformation or shape change at high strain rates.

Ultrafast laser-driven shock waves ~ 5 GPa pressure were used to study molecular orientational processes occurring in a thin layer of polycrystalline energetic material [74]. It was observed that there is an orientational sensitivity of energetic materials to the direction of shock front propagation. Recovery experiments, where the shocked material sample is examined after the shock, are ordinarily limited to refractory materials, which can withstand high pressure conditions. It is difficult to recover molecular energetic materials at substantial shock loads, since long-duration shocks usually explode the energetic material. The nanoshock technique is uniquely suited for recovery measurements of high explosives. The duration of the shock pulse is so short (few nanoseconds) that there is little time for thermo-chemical decomposition reaction to take place.

Experiments have been done to probe material properties using ISTS detection under gas gun shock loading on glycerol [75]. Preliminary results show distinct, large changes in acoustic frequency under shock loading. Analysis is still under way but experiments can only proceed at one shot every few days. CARS and ISTS are both coherent vibrational spectroscopies, the former measuring localized, molecular vibrational modes on femtosecond–picosecond time scales and the latter measuring collective, acoustic vibrational modes on nanosecond time scales. Both molecular and collective responses to shock are of great interest. Recent CARS results on molecular vibrational evolution under shock conditions suggest the value and complementarity of ISTS measurements.

4.3 ISTS measurements under laser shock loading

So far, we have discussed ISTS measurements (in Chapter 2) and shock generation (in Chapter 3) separately. This section presents their integration and shows preliminary demonstration of measurements on samples under laser-induced shock loading using ISTS as detection technique.

4.3.1 Experimental Technique

The two main components of the experiment are laser shock generation, achieved through intense pulsed ablation of a metal film at the backside of the sample, and ISTS photoacoustic measurement of mechanical properties, achieved through mild spatially periodic heating and time-resolved observation of acoustic waves at the front side.

Figure 4-5 shows the schematic illustration of the ISTS measurement with the excitation and probe beams and the signal on one side of a sample (right-hand side excitation pulses, probe, and diffracted signal) and laser shock generation at the opposite side (left-hand side shock pulse). The sample of interest is typically a polymer layer surrounded by metal layers that are irradiated for shock generation (Al layer) and for acoustic wave generation and probing (Au layer). The time-dependent acoustic response yields the sample dynamic mechanical properties before, during, and after shock loading.

In our case the shock generation pulse has a fast ($\sim$200 fs) rise and a gradual ($\sim$300 ps) decay so that the resulting shock wave may have a similar profile, thereby maintaining shock pressure for an extended duration. This intense pulse (800 nm, 700 μJ focused to 125 μm spot diameter) strikes an aluminum film and creates a plasma that launches the shock wave into the sample material. The expansion (along

POLYMER 1-10 μm

Aluminium Ablation Layer ~2 μm

Gold Overlayer ~0.4-1 μm

Diffracted Probe Beam (Detector)

Sapphire (0.5-2mm) / BK7 Glass (100-200 μm)

Excitation pulses (ISTS Pump - 400 nm, 150-250 fs, 50 Hz)

interferometer

Shock pulse – 810 nm, 100-200 ps, 1 Hz, Variable Delay

CCD

Probe Pulse (Continuous, 532 nm)

BACKSIDE: SHOCK   FRONTSIDE: ISTS

$\hat{x}$ $\hat{y}$ $\hat{z}$
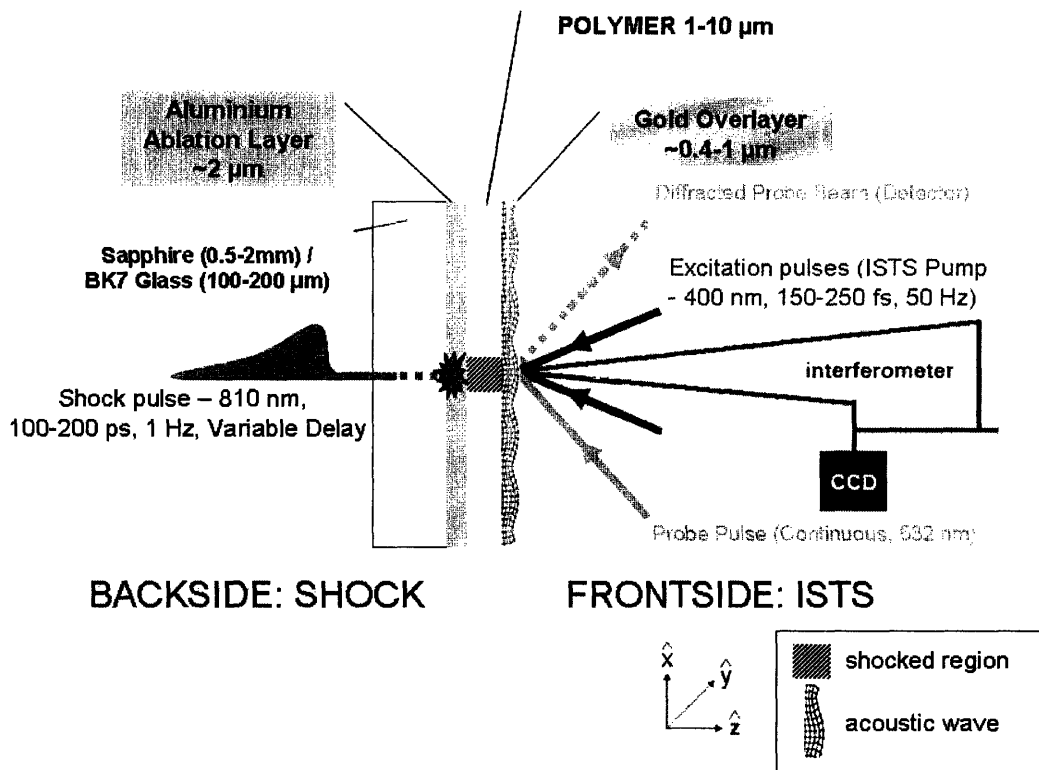
shocked region

acoustic wave

Figure 4-5: Sample geometry for the shock experiment. This schematic shows the sample assembly, shocked region, ISTS pump and probe beams, and the interferometer. The acoustic wave is generated by ISTS in the gold layer but extends throughout the polymer sample whose time-dependent response to the shock can therefore be monitored.

$\hat{z}$ direction) of the aluminum film drives a mechanical shock wave into the adjacent polymer layer since it is much softer than the rigid glass/sapphire substrate [76]. For laser generated planar shock waves, the diameter of the spot must be at least ten times the run distance.

Laser ablation consists of three coupled processes [77]:

1. heat conduction within the solid governed by Laplace's equations

2. flow through a discontinuity layer attached to the solid surface

3. shock wave expansion of the laser induced plume

The shock pulse may be shaped and optimized in order to generate a shock response with a specified temporal profile. The shock induces a surface displacement along $\hat{z}$, which can be detected by measuring the change in the phase (i.e. optical path delay) between the two arms of the Mach-Zehnder interferometer (see Chapter 3 for details).

The excitation and probe laser light used for the ISTS measurement strike a gold film on the opposite side of the sample. Although the light pulses do not penetrate the gold film layer, the acoustic response that they generate persists throughout this layer and the sample of interest beneath it, and the acoustic properties therefore reveal the mechanical properties of the sample. If a shock wave is launched, then changes in the acoustic behavior may be observed as the sample undergoes time-dependent changes due to shock loading.

Laser-driven shocks are generated at a rate of 1 shot/sec, and the sample is rastered along $\hat{x}\hat{y}$–plane to ensure that an undamaged region is irradiated each time. In a sample of 1" diameter, over a thousand shots can be conducted in a few minutes. This presents a huge advantage over ISTS measurements under way in parallel,

collaborative experiments at Washington State University on samples under gas gun shock loading, in which the entire sample, not just a small region, is destroyed in a single shot and at most a few shots per week are practical.

Each of the ISTS traces recorded from a single shot contains the entire time-dependent response, typically showing acoustic oscillations that continue for several tens of nanoseconds. Varying the time delay between the shock and ISTS excitation pulses produces a map of the temporal response over a window hundreds of nanoseconds wide, ranging from before to well after the sample is shocked. A translation of a phase mask changes the acoustic wave vector of the grating, enabling the complete acoustic dispersion relation $[\omega(\vec{k})]$ to be determined under these unique shock-loading conditions.

Measurements were made on the neat and polyhedral oligomeric silsesquioxane (POSS) doped poly(methyl methacrylate) (PMMA) as well as on PMMA–polyisoprene (PI) block copolymer thin films under shock conditions. The material and sample details are presented in Chapter 2.

4.3.2   Preliminary Results and Discussion

Figure 4-6 shows the first results of ISTS measurements on samples that have been subjected to laser shock loading. Small-amplitude shocks have been used for the initial demonstration, but the method is now applicable to widely varying shock amplitudes including those far above the threshold for irreversible sample damage. The results permit direct observation of the effects of shock loading on time-dependent mechanical properties as revealed through the measured acoustic behavior. Shock wave reverberations through the sample and acoustic signals from the samples before, during, and after shock loading are observed. It should be emphasized that these
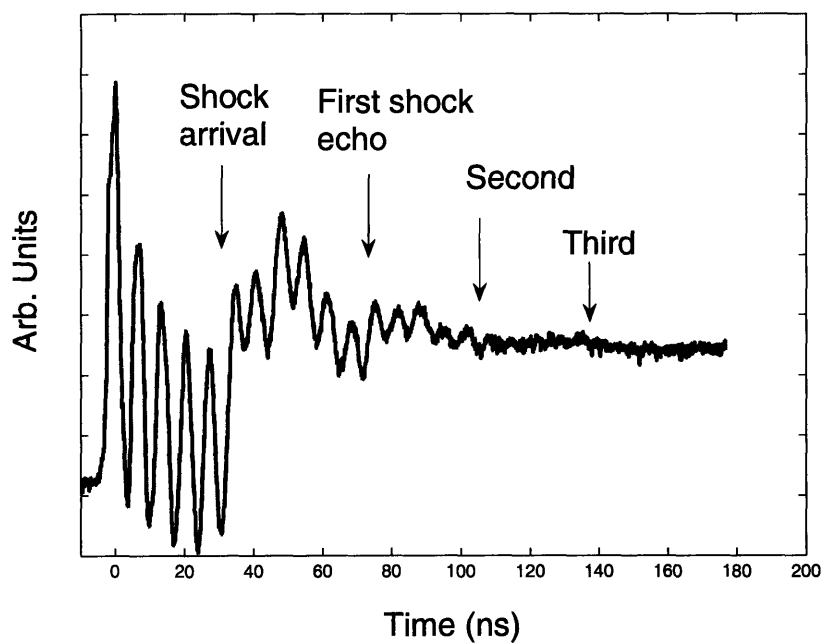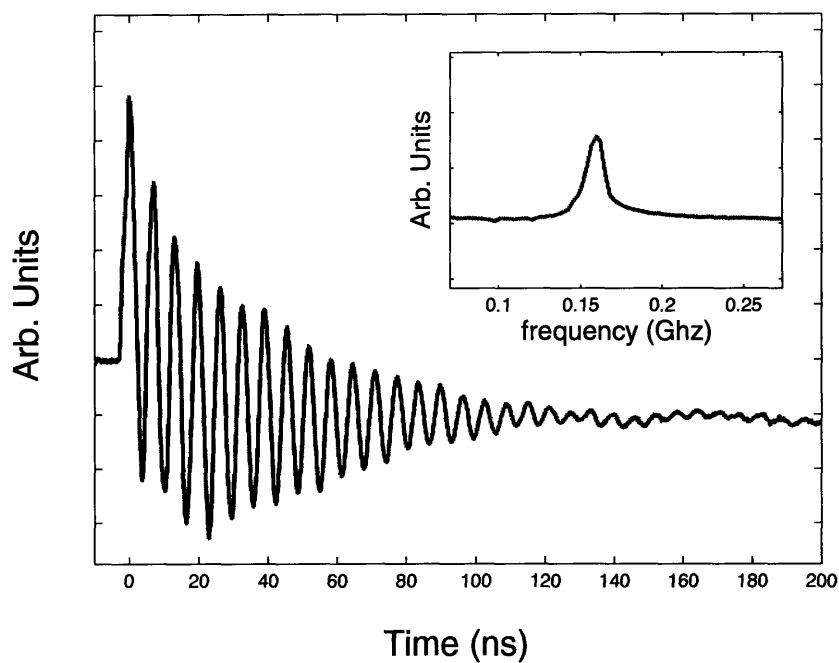
Figure 4-6: Top: ISTS data from 4.3 μm wavelength acoustic responses in a 1.1 μm film of 5 wt% POSS doped PMMA in unshocked state. Bottom: Averaged ISTS data during shock propagation. The averaged data are recorded on a single shot basis, moving to a new sample location for each of the 15 shots. The echoes recorded in the sample correspond to the reverberation of the shock pulses in the glass substrate.
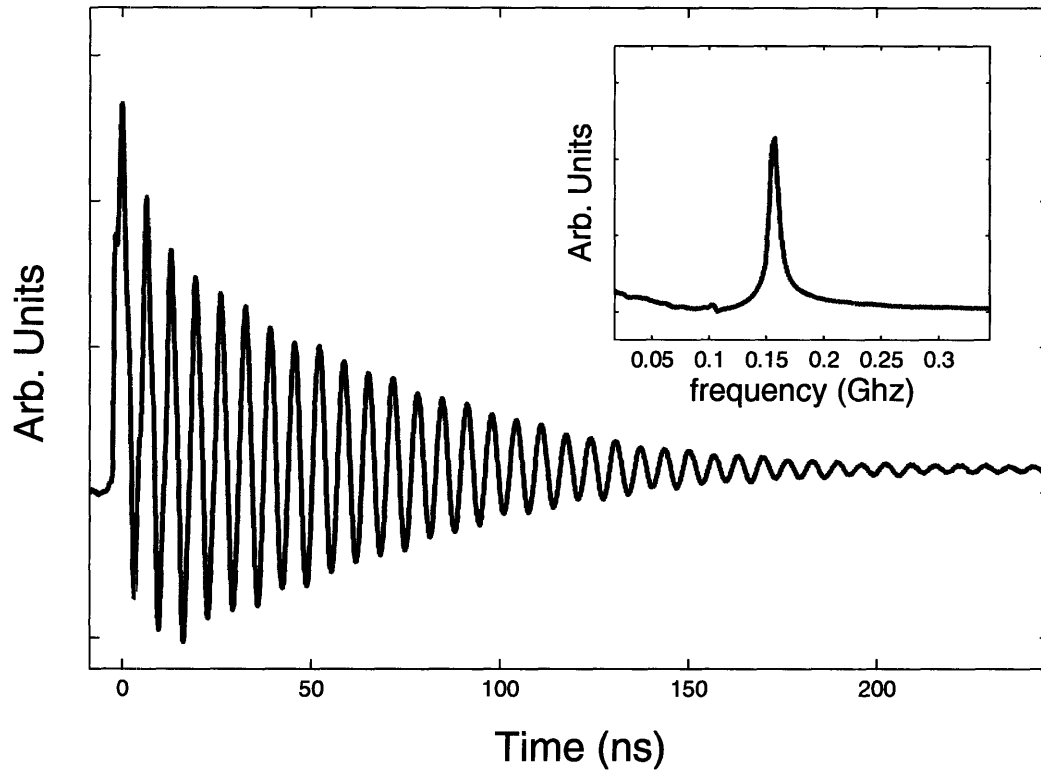
Figure 4-7: Averaged ISTS data from 4.3 μm wavelength acoustic responses in a 1.1 μm film of 5 wt% POSS doped PMMA at long times after shock that was below the sample damage threshold.

measurements, the first of their kind, are applicable to a very wide range of single-component and composite materials.

The ISTS measurements with a synchronized shock pulse are shown in Figures 4-6 and 4-9. The results shown were accumulated by averaging several single-shot measurements. Although the shock typically leads to irreversible damage of the sample after several shots at the same region, it is practical to average signals from different spots on a spin-coated or otherwise deposited polymer film of good quality and uniformity. The shock pulse is focused a spot size of about 100 microns at the sample, so only a small area of the polymer layer is damaged on each shot. The shock wave reverberations within the sample could be exploited to prolong its excursion to elevated pressure, potentially permitting study of high-pressure steady states that normally are only accessible in gas gun shock loading measurements. The method may be applied to individual material components of complex assemblies to assess their intrinsic behavior under extreme conditions and to the assemblies themselves to assess their collective performance.

At the low shock pulse amplitude used, which was below the single shot sample damage threshold, there is no marked change in the time-domain signal or the Fourier transform before and after the shock in the ISTS data from 4.3 μm wavelength acoustic responses in a 1.1 μm film of with 5 wt% POSS doped PMMA (compare Figures 4-6 and 4-7). In this case the polymer is not irreversibly changed during shock loading. The shock acoustic echoes recorded in the sample correspond to the time of flight in the glass substrate for one round trip of the reflected shock at the glass/aluminum interface.

The dynamics of the shock initial arrival and echoes through the sample are shown through reflectivity measurements as illustrated in Figure 4-9. These permit characterization of the shock dynamics separate from evaluation of sample mechanical

76
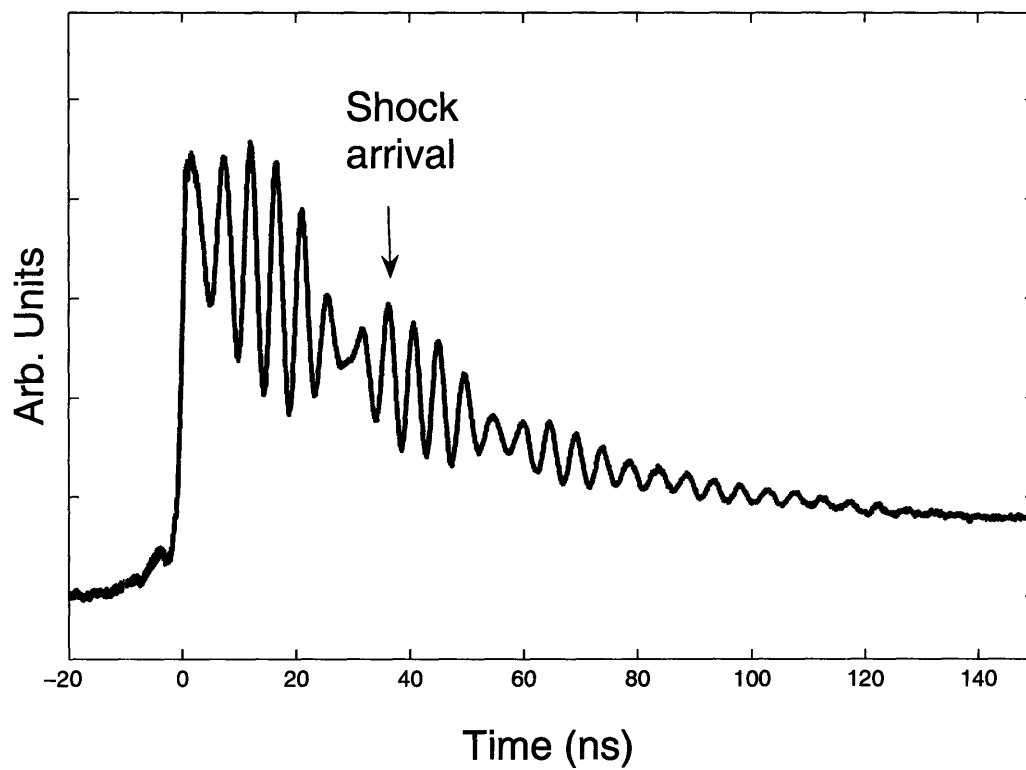
Figure 4-8: Averaged ISTS data of PMMA–Polyisoprene block copolymer for shock pulse just below damage threshold. Data are recorded on a single-shot basis. The frame shows the average of 25 signals recorded from different spots on the sample.
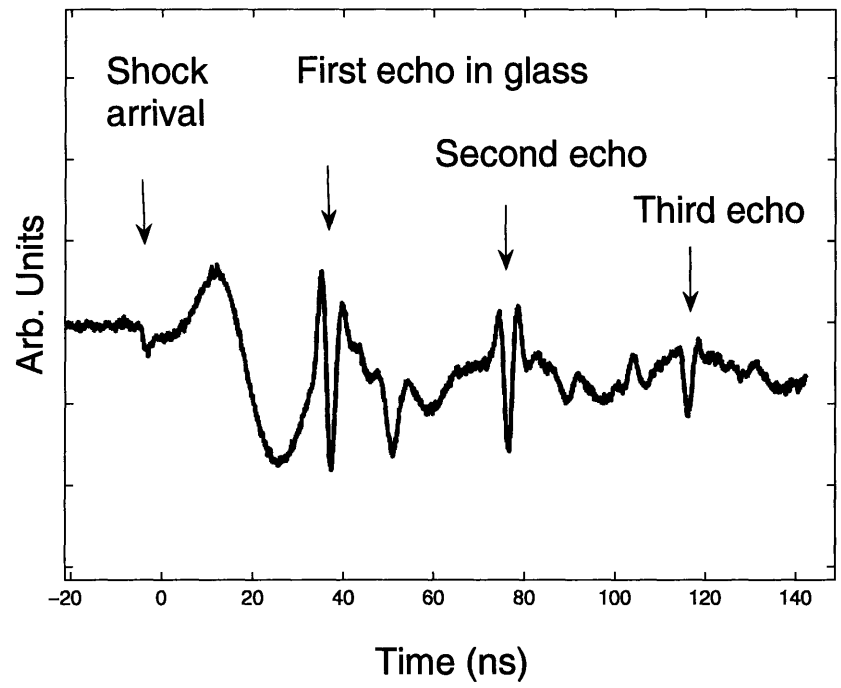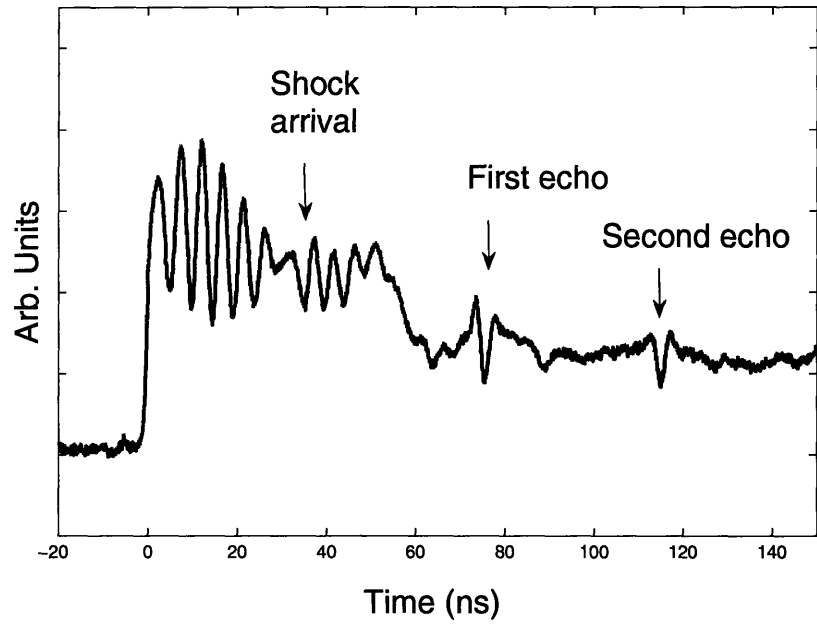
Figure 4-9: Top: Averaged ISTS data during shocked state from 8.6 μm wavelength acoustic responses in a 130 nm film of PMMA–PI block copolymer that had been annealed for 5 hours. Bottom: Averaged single shot reflectivity data (not ISTS) of shocked sample. This record attest the presence of several acoustical shock echoes traveling back and force inside the structure formed by the glass substrate and the top polymer.

properties and their evolution.

Thus, we can make ISTS measurements on laser shocked samples. Extended sample structure with solid substrate on gold layer will permit far higher shock amplitudes that will yield measurable acoustic frequency changes in ISTS detection. Interferometry will be conducted on shocks that we generate so as to characterize shock pressure and density.

Chapter 5

Summary

5.1 Conclusions

Impulsive stimulated thermal scattering (ISTS) photoacoustic measurements have been conducted on novel structures to characterize interesting polymer and multilayer samples. These measurements were performed on complex polymeric materials – neat and polyhedral oligomeric silsesquioxane (POSS) doped poly(methyl methacrylate) (PMMA), PMMA–Polyisoprene (PMMA-b-PI) block copolymer, nanocrystalline materials such as TiO_2 and a PMMA–TiO_2 multilayer film.

The measurements were conducted with various acoustic wavelengths and corresponding frequencies in order to extract the full set of acoustic and modulus parameters. The results already illustrate the general value of ISTS measurements for revealing the effects of processing conditions on dynamic mechanical behavior of nanostructured polymers. Acoustic properties of the multilayer structure indicating very low group velocity in high-wavevector range and strong dispersion in the group velocity at higher frequencies suggest possible material which could be used for shock mitigation.

Laser-induced shock loading has been synchronized with ISTS laser generation and measurement of acoustic waves through ISTS so that dynamical evolution of mechanical properties in shocked materials can be examined. This is of crucial importance in understanding the performance of protective materials under shock loading conditions, and is possible with small quantities of materials that are still under development in order to guide their optimization. These measurements will be of fundamental interest and will provide the static and dynamic material parameters needed for interpretation of the next set of measurements on nanostructured polymeric systems.

5.2 Future Directions

Advanced multicomponent material systems including block copolymers, multilayer assemblies, self-assembled composites, and others may undergo extremely complex responses to shock including phase separation or transitions, plastic deformation and cracking, delamination, chemical degradation, etc. Direct real-time measurement of mechanical responses during the shock event can reveal failure mechanisms and dynamics that may then be addressed systematically through optimization of individual component performance under impact and optimization of composite phononic properties including tailored reflection, scattering and damping of shock wave components. This thesis has presented an experimental protocol for assessment of performance under shock loading. The results presented foreshadow more routine measurement of laser shock dynamics in which the shock and the material response to it are characterized.

A wide variety of candidate armor materials including energy-absorbing, complex heterogeneous polymeric nanocomposites, will be characterized using this technique.
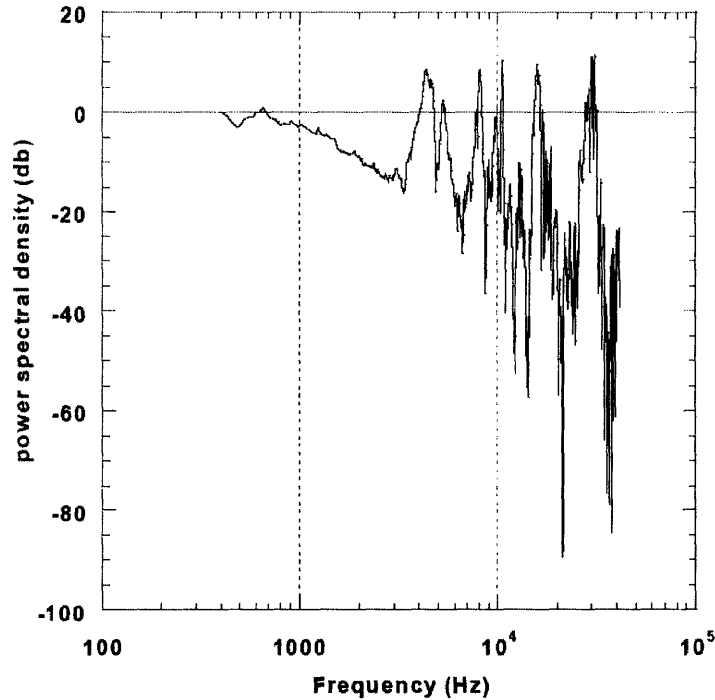
Figure 5-1: Power spectral density as a function of frequency experienced by an unprotected mannequin facing detonation of 100 grams of military plastic C4 explosive [78].

Research has shown that the physical properties of a given polymer may be dramatically altered by the introduction of a secondary nano-scale particulate phase, even at very low weight percent. Typical materials for this investigation will be systems that show promise of heightened energy absorption, deflection, and reflection under shock-loading. Systems will be chosen to take advantage of mechanisms such as filler-toughening, amorphization, chain scission, activated flow, and melting. Being able to directly measure the temporal development of the mechanical properties of a polymer will indicate transitions and dynamical behavior within the material. Depending on the characteristic material behavior, the moduli may increase or decrease. Some viscous materials jam under high strain rates; whereas, others can exhibit flow.

The power spectrum of a typical blast is broad, with spectral components rep-

resenting destructive energy present between 1 and 20 kHz (see Figure 5-1). Efforts to mitigate blast could attempt to attenuate, reflect, or generally control the most damaging part of the spectrum. Methods of fabricating two-dimensionally periodic *phononic crystals* – band gap structures designed to forbid the propagation of specific acoustic modes - are being developed [25, 79]. Examining the shocked response of such structures with band gaps coinciding with shock frequencies will be a promising advance toward potential blast mitigation. In laser shock measurements, the power spectrum lies at far higher frequencies and correspondingly shorter wavelength ranges. The mitigation principles learned from laser shock measurements should be scalable to the ranges appropriate for ballistic or blast mitigation.

Thus, systematic characterization of polymer nanocomposite shock responses as a function of nanocomposite properties, shock pressure and duration as well as examination of acoustic properties in multilayered materials and phononic bandgap materials with nanometer-scale structures and heterogeneities will provide insight into possible unique energy dissipation pathways available in new polymer based and nanocomposite materials. Interferometric measurements will allow to characterize the shock pulse pressure present in a material as a function of time, with sub-picosecond resolution, as the shock wave propagates through the sample. Ultimately, all of the collected spectroscopic information will combined with a theoretical modeling effort to provide a complete picture of the modes of energy dissipation present in the materials being studied.

Bibliography

[1] M. A. Meyers. *Dynamic Behavior of Materials*. John Wiley and Sons, Inc., New York, 1994.

[2] H. Maris. *Picosecond Ultrasonics*. Scientific American, 278(1):86–89, 1998.

[3] N. A. Vachhani. *Using Narrowband Pulse-shaping to Characterize Polymer Structure and Dynamics: Deathstar GHz Spectroscopy*. SM Thesis, Massachusetts Institute of Technology, Department of Materials Science and Engineering, 2005.

[4] J. A. Rogers. *Time-resolved Photoacoustic and Photothermal Measurements on Surfaces, Thin Films and Multilayer Assemblies*. Ph.D. Thesis, Massachusetts Institute of Technology, Department of Chemistry, 1995.

[5] T. F. Crimmins. *Ultrahigh Frequency Characterization of Complex Materials using Transient Grating Techniques*. Ph.D. Thesis, Massachusetts Institute of Technology, Department of Chemistry, June 2000.

[6] A. A. Maznev, J. A. Rogers, and K. A. Nelson. *Optical Heterodyne Detection of Laser-induced Gratingss*. Optic Letters, 23: 1319–1321, 1998.

[7] R. M. Slayton, K. A. Nelson, and A. A. Maznev. *Transient Grating Measurements of Film Thickness in Multilayer Metal Films. Journal Of Applied Physics*, 90(9): 4392–4402, 2001.

[8] Dhar L. Rogers, J. A. and K. A. Nelson. *Noncontact Determination of Transverse Isotropic Elastic Moduli in Polyimide Thin Films using a Laser based Ultrasonic Method. Applied Physics Letters*, 65: 312–314, 1994.

[9] J. A. Rogers, A. A. Maznev, M. J. Banet, and K. A. Nelson. *Optical Generation and Characterization of Acoustic Waves in Thin Films: Fundamentals and Applications. Annual Review Of Materials Science*, 30: 117–157, 2000.

[10] J. A. Rogers. *Real Time Impulsive Stimulated Thermal Scattering of Thin Polymer Films*. SM Thesis, Massachusetts Institute of Technology, Department of Chemistry, 1992.

[11] Y. X. Yan. Ph.D. Thesis, Massachusetts Institute of Technology, Department of Physics, 1988.

[12] Y.-X. Yan and K. A. Nelson. *Impulsive Stimulated Light Scattering. I. General Theory. Journal of Chemical Physics*, 87: 6240–6256, 1987.

[13] Y.-X. Yan and K. A. Nelson. *Impulsive Stimulated Light Scattering. II. Comparison to Frequency-domain Light Scattering Spectroscopy. Journal of Chemical Physics*, 87: 6257–6265, 1987.

[14] A. R. Duggal, J. A. Rogers, and K. A. Nelson. *Real-Time Optical Characterization Of Surface Acoustic Modes Of Polyimide Thin-Film Coatings. Journal Of Applied Physics*, 72(7): 2823–2839, 1992.

[15] A. R. Duggal, J. A. Rogers, K. A. Nelson, and M. Rothschild. *Real-time Characterization of Acoustic Modes of Polyimide Thin Film Coatings using Impulsive Stimulated Thermal Light Scattering*. Applied Physics Letters, 60: 692–694, 1992.

[16] Y. W. Yang, K. A. Nelson, and F. Adibi. *Optical Measurement of the Elastic-moduli and Thermal Diffusivity of a C-N Film*. Journal of Materials Research, 10(1): 41–48, 1995.

[17] R.W. Hertzberg. *Deformation and Fracture Mechanics of Engineering Materials*. John Wiley and Sons, New York, 4th edition, 1996.

[18] C.J. Morath and H.J. Maris. *Phonon Attenuation in Amorphous Solids Studied by Picosecond Ultrasonics*. Physical Review B, 54(1):203–213, 1996.

[19] M. Sinha. *Probing Polymer Networks Using Pulse Propagation and Brillouin Light Scattering Techniques*. Ph.D. Thesis, University of Cincinnati, 2000.

[20] S. Silence. *Time-resolved Light Scattering Studies of Structural Rearrangements in Disordered Condensed Phase Systems*. Ph.D. Thesis, Massachusetts Institute of Technology, Department of Chemistry, 1991.

[21] L. Chazeau, C. Gauthier, G. Vigier, and J. Y. Cavaille. *Relationship Between Microstructural Aspects and Mechanical Properties of Polymer-based Nanocomposites*. Handbook of Organic-Inorganic Hybrid Materials and Nanocomposites, 2: 63–111, 2003.

[22] F. Mammeri, E. Le Bourhis, L. Rozes, and C. Sanchez. *Mechanical Properties of Hybrid Organic-inorganic Materials*. Journal of Materials Chemistry, 15: 3787–3811, 2005.

[23] Impact Analytical, http://www.impactanalytical.com/dsc.html and University of Missouri-Rolla, http://web.umr.edu/~wlf/Bulk/Andrews.html.

[24] J. Yoon, W. Lee, J. M. Caruge, M. Bawendi, E. L. Thomas, S. Kooi, and P. Prasad. *Defect-mode Mirrorless Lasing in Dye-doped Organic/Inorganic Hybrid One-dimensional Photonic Crystal. Applied Physics Letters*, 88, 2006.

[25] T. Gorishnyy, C.K. Ullal, M. Maldovan, G. Fytas, and E.L. Thomas. *Hypersonic Phononic Crystals. Physical Review Letters*, 94:115501/1–115501/4, 2005.

[26] G. Lu and T. X. Yu. *Energy Absorption of Structures and Materials*. Cambridge : Woodhead Publications, Boca Raton : CRC Press, 2003.

[27] S. Y. Soong, R. E. Cohen, M. C. Boyce, and A. D. Mulliken. *Rate-dependent Deformation Behavior of POSS-filled and Plasticized Poly(vinyl chloride). Macromolecules*, 39(8):2900–2908, 2006.

[28] S.H. Phillips, T.S. Haddad, and S.J. Tomczak. *Developments in Nanoscience: Polyhedral Oligomeric Silsesquioxane (POSS)-Polymers. Current Opinion in Solid State and Materials Science*, 8(1):21–29, 2004.

[29] E. Scolan and C. Sanchez. *Energy Absorption of Structures and Materials. Chem. Mater.*, 10:3217, 1998.

[30] NDT Resource Center, http://www.ndt-ed.org/EducationResources/.

[31] O. A. Hasan, M. C. Boyce, X. S. Li, and S. Berko. *An Investigation of the Yield and Postyield Behavior and Corresponding Structure of Poly(methyl methacrylate). Journal of Polymer Science Part B: Polymer Physics*, 31:185–197, 1993.

[32] Intelligent Work Forums for Engineering Professionals, http://www.eng-tips.com/viewthread.cfm?qid=120480.

[33] D. B. Drazkowski, A. Lee, T. S. Haddad, and D. J. Cookson. *Chemical Substituent Effects on Morphological Transitions in Styrene-Butadiene-Styrene Triblock Copolymer Grafted with Polyhedral Oligomeric Silsesquioxanes.* *Macromolecules*, 39(5):1854–1863, 2006.

[34] E. T. Kopesky, G. H. McKinley, and R. E. Cohen. *Toughened Poly(methyl methacrylate) Nanocomposites by Incorporating Polyhedral Oligomeric Silsesquioxanes.* *Polymer*, 47(1):299–309, 2006.

[35] E. T. Kopesky, T. S. Haddad, R. E. Cohen, and G. H. McKinley. *Thermomechanical Properties of Poly(methyl methacrylate)s Containing Tethered and Untethered Polyhedral Oligomeric Silsesquioxanes.* *Macromolecules*, 37(24):8992–9004, 2004.

[36] A. D. Mulliken. *Mechanics of Amorphous Polymers and Polymer Nanocomposites during High Rate Deformation.* Ph.D. Thesis, Massachusetts Institute of Technology, Department of Mechanical Engineering, 2006.

[37] Archie P. Smith, Harald Ade, Carl C. Koch, Steven D. Smith, and Richard J. Spontak. *Addition of a Block Copolymer to Polymer Blends Produced by Cryogenic Mechanical Alloying.* *Macromolecules*, 33(4):1163–1172, 2000.

[38] D. B. Hayes. *Introduction to Stress Wave Phenomena.* Sandia National Laboratories, Albuquerque, 1973.

[39] D. D. Dlott. *Ultrafast spectroscopy of shock waves in molecular materials.* *Annual Review Of Physical Chemistry*, 50: 251–278, 1999.

[40] D. D. Dlott. *Ultrafast Spectroscopy of Shock Waves in Molecular Materials.* *Annual Review of Physical Chemistry*, 50: 251–278, 1999.

[41] D. D. Dlott. *Nanoshocks in molecular materials. Accounts Of Chemical Research*, 33(1): 37–45, 2000.

[42] S. M. Walley, J. E. Field, P. H. Pope, and N. A. Safford. *The Rapid Deformation-Behavior Of Various Polymers. Journal De Physique Iii*, 1(12):1889–1925, 1991.

[43] J. Dunn, D. F. Price, S. J. Moon, R. C. Cauble, P. T. Springer, and A. Ng. *1-10 Mbar Laser-driven Shocks using the Janus Laser Facility. AIP Conference Proceedings*, 620(2):1371, 2002.

[44] T. J. Ahrens. *Rock Physics and Phase Relations*, volume 3, chapter Shock Wave Data for Rocks, pages 35–44. American Geophysical Union, 1995.

[45] R. Evans, A.D. Badger, F. Fallies, M. Mahdieh, T.A. Hall, P. Audebert, J.-P. Geindre, J.-C. Gauthier, A. Mysyrowicz, G. Grillon, and A. Antonetti. *Time-and Space-resolved Optical Probing of Femtosecond-laser-driven Shock Waves in Aluminum. Physical Review Letters*, 77(16):3359–3362, 1996.

[46] K. T. Gahagan, D. S. Moore, D. J. Funk, J. H. Reho, and R. L. Rabie. *Ultra-fast Interferometric Microscopy for Laser-driven Shock Wave Characterization. Journal Of Applied Physics*, 92(7):3679–3682, 2002.

[47] D. J. Funk, D. S. Moore, K. T. Gahagan, S. J. Buelow, J. H. Reho, G. L. Fisher, and R. L. Rabie. *Ultrafast Measurement of the Optical Properties of Aluminum during Shock-wave Breakout. Physical Review B*, 6411(11), 2001.

[48] S.D. McGrane, D.S. Moore, and D.J. Funk. *Ultrafast Spectroscopy and Interferometry of Laser-shocked Thin Films: Practical Considerations. Proceedings of the SPIE - The International Society for Optical Engineering*, 5448(1):165–170, 2004.

90

[49] T. de Rességuier, S. Couturier, M. Boustie, J. David, G. Nierat, and F. Bauer. *Characterization of Laser-driven Shocks of High Intensity using Piezoelectric Polymers. Journal Of Applied Physics*, 80(7):3656–3661, 1996.

[50] D. J. Funk, D. S. Moore, S. D. McGrane, K. T. Gahagan, J. H. Reho, S. J. Buelow, J. Nicholson, G. L. Fisher, and R. L. Rabie. *Ultrafast Studies of Shock Waves using Interferometric Methods and Transient Infrared Absorption Spectroscopy. Thin Solid Films*, 453-54:542–549, 2004.

[51] D. S. Moore, D. J. Funk, K. T. Gahagan, J. H. Reho, G. L. Fisher, S. D. McGrane, and R. L. Rabie. *Sub-picosecond Laser-driven Shocks in Metals and Energetic Materials. AIP Conference Proceedings*, 620(pt.2):1333, 2002.

[52] J. P. Geindre, P. Audebert, A. Rousse, F. Fallies, J. C. Gauthier, A. Mysyrowicz, A. Dossantos, and G. Hamoniaux. *Frequency-Domain Interferometer for Measuring the Phase and Amplitude of a Femtosecond Pulse Probing a Laser-Produced Plasma. Optics Letters*, 19(23):1997–1999, 1994.

[53] D. S. Moore, K. T. Gahagan, S. J. Buelow, R. L. Rabie, D. J. Funk, S. A. Sheffield, L. L. Davis, T. Lippert, H. Brand, and J. W. Nicholson. *Time- and Space-resolved Optical Probing of the Shock Rise Time in Thin Aluminum Films. AIP Conference Proceedings*, 505(pt.2):1003, 2000.

[54] D. J. Funk, D. S. Moore, S. D. McGrane, J. H. Reho, and R. L. Rabie. *Ultra-fast Spatial Interferometry: A Tool for Characterizing Material Phase and Hydrodynamic Motion in Laser-excited Metals. Applied Physics A-Materials Science and Processing*, 81(2):295–302, 2005.

91

[55] K. T. Gahagan, J. H. Reho, D. S. Moore, D. J. Funk, and R. L. Rabie. *Ultrafast Time-resolved 2D Spatial Interferometry for Shock Wave Characterization in Metal Films. AIP Conference Proceedings*, 620(pt.2):1351–1354, 2002.

[56] D.J. Funk, D.S. Moore, J.H. Reho, K.T. Gahagan, S.D. McGrane, and R.L. Rabie. *Ultrafast Measurement of the Optical Properties of Shocked Nickel and Laser Heated Gold. AIP Conference Proceedings*, (620):1227–1230, 2002.

[57] D. S. Moore, K. T. Gahagan, J. H. Reho, D. J. Funk, S. J. Buelow, R. L. Rabie, and T. Lippert. *Ultrafast Nonlinear Optical Method for Generation of Planar Shocks. Applied Physics Letters*, 78(1):40–42, 2001.

[58] S. D. McGrane, D. S. Moore, D. J. Funk, and R. L. Rabie. *Spectrally Modified Chirped Pulse Generation of Sustained Shock Waves. Applied Physics Letters*, 80(21):3919–3921, 2002.

[59] K. T. Gahagan, D. S. Moore, D. J. Funk, R. L. Rabie, S. J. Buelow, and J. W. Nicholson. *Measurement of Shock Wave Rise Times in Metal Thin Films. Physical Review Letters*, 85(15):3205–3208, 2000.

[60] S. P. Marsh. *LASL Shock Hugoniot Data.* University of California, Berkeley, CA, 1980.

[61] S. D. McGrane, D. S. Moore, and D. J. Funk. *Sub-picosecond Shock Interferometry of Transparent Thin Films. Journal Of Applied Physics*, 93(9):5063–5068, 2003.

[62] S.D. McGrane, D.S. Moore, and D.J. Funk. *Measurement of Shocked Thin Polymer Film Hugoniot Properties with Ultrafast Dynamic Ellipsometry. AIP Conference Proceedings*, (706):1181–1186, 2004.

[63] Y. M. Gupta. *Determination Of The Impact Response Of PMMA Using Combined Compression And Shear Loading. Journal Of Applied Physics*, 51(10):5352–5361, 1980.

[64] D. D. Dlott, S. Hambir, and J. Franken. *The New Wave in Shock Waves. Journal of Physical Chemistry B*, 102(12):2121–2130, 1998.

[65] K. G. Nakamura, K. Wakabayashi, and K. Kondo. *Transient Bond Scission of Polytetrafluoroethylene under Laser-induced Shock Compression studied by Nanosecond Time-resolved Raman spectroscopy. AIP Conference Proceedings*, 620(2):1259, 2002.

[66] A. Matsuda, K. G. Nakamura, and K. Kondo. *Time-resolved Raman Spectroscopy of Benzene and Cyclohexane under Laser-driven Shock Compression. Physical Review B*, 65(17), 2002.

[67] H. Kim, S. A. Hambir, and D. D. Dlott. *Ultrafast High Repetition Rate Absorption Spectroscopy of Polymer Shock Compression. Shock Waves*, 12(1):79–86, 2002.

[68] S.A. Hambir, J. Franken, D.E. Hare, E.L. Chronister, B.J. Baer, and D.D. Dlott. *Ultrahigh Time-resolution Vibrational Spectroscopy of Shocked Molecular Solids. Journal of Applied Physics*, 81(5):2157–2166, 1997.

[69] S. A. Hambir, H. Kim, and D. D. Dlott. *Ultrafast Dynamics of Nanoshocks in Molecular Materials. AIP Conference Proceedings*, 505(pt.2):945, 2000.

[70] D. E. Hare, J. Franken, D. D. Dlott, E. L. Chronister, and J. J. Flores. *Dynamics of a Polymer Shock Optical Microgauge Studied by picosecond Coherent Raman-Spectroscopy. Applied Physics Letters*, 65(24):3051–3053, 1994.

[71] G. Tas, S. A. Hambir, J. Franken, D. E. Hare, and D. D. Dlott. *Coherent Raman Spectroscopy of Nanoshocks. Journal Of Applied Physics*, 82(3):1080–1087, 1997.

[72] S. A. Hambir, J. Franken, D. E. Hare, E. L. Chronister, B. J. Baer, and D. D. Dlott. *Ultrahigh Time-resolution Vibrational Spectroscopy of Shocked Molecular Solids. Journal Of Applied Physics*, 81(5):2157–2166, 1997.

[73] A. S. Lagutchev, J. E. Patterson, W. T. Huang, and D. D. Dlott. *Ultrafast Dynamics of Self-assembled Monolayers under Shock Compression: Effects of Molecular and Substrate Structure. Journal Of Physical Chemistry B*, 109(11):5033–5044, 2005.

[74] J. Franken, S. A. Hambir, and D. D. Dlott. *Ultrafast Shock-induced Orientation of Polycrystalline Films: Applications to High Explosives. Journal Of Applied Physics*, 85(4):2068–2074, 1999.

[75] Naoki Hemmi (Washington State University) and Darius H.Torchinsky (Massachusetts Institute of Technology), August, 2005.

[76] I. Y. S. Lee, J. R. Hill, H. Suzuki, D. D. Dlott, B. J. Baer, and E. L. Chronister. *Molecular-Dynamics Observed 60 ps behind a Solid-State Shock Front. Journal of Chemical Physics*, 103(19):8313–8321, 1995.

[77] Zhaoyan Zhang and G. Gogos. *Theory of Shock Wave Propagation During Laser Ablation. Physical Review B (Condensed Matter and Materials Physics)*, 69(23):235403-1–235403-9, 2004.

[78] A. Makris, J. Nerenberg, J.P. Dionne, C.R. Bass, and C. Chichester. *Reduction of Blast Induced Head Acceleration in the Field of Anti-Personnel Mine Clearance.* 2001.

94

[79] E.J. Reed, M. Soljaccic, and J.D. Joannopoulos. *Color of Shock Waves in Photonic Crystals. Physical Review Letters*, 90:203904, 2003.